Where infall meets outflows: turbulent dissipation probed by CH+ and Lyα in the starburst/AGN galaxy group SMM J02399–0136 at z ∼ 2.8

A Vidal-García, E Falgarone, F Arrigoni battaia, B Godard, R J Ivison, M A Zwaan, C Herrera, D Frayer, P Andreani, Q Li, et al.

Where infall meets outflows: turbulent dissipation probed by CH⁺ and Lyα in the starburst/AGN galaxy group SMM J02399−0136 at z ∼ 2.8

A. Vidal-García,[1]★ E. Falgarone,[1]★ F. Arrigoni Battaia,[2] B. Godard,[1,3] R. J. Ivison [4] M. A. Zwaan,[4]
C. Herrera,[5] D. Frayer,[6] P. Andreani [4] Q. Li[7] and R. Gavazzi[8]

[1]*LPENS, Ecole Normale Supérieure, Université PSL, CNRS, Sorbonne Université, Université Paris-Diderot, 75005, Paris, France*
[2]*Max-Planck-Institute für Astrophysik, Karl-Schwarzschild-Strasse 1, D-85748 Garching bei München, Germany*
[3]*Observatoire de Paris, Ecole Normale Supérieure, Université PSL, Sorbonne Université, CNRS LERMA, 75014, Paris, France*
[4]*European Southern Observatory, Karl-Schwarzschild-Strasse 2, D-85748 Garching bei München, Germany*
[5]*Institut de radioastronomie millimétrique, 106 rue de la Piscine, 38400, Saint Martin d'Hères, France*
[6]*Green Bank Observatory, PO Box 2, Green Bank, WV 24944, USA*
[7]*Kavli Institute for Astronomy and Astrophysics, Peking University, Beijing, 100871, People's Republic of China*
[8]*Sorbonne Université, CNRS, UMR7095, Institut d'Astrophysique de Paris, F-75014 Paris, France*

ABSTRACT

We present a comparative analysis of the CH⁺(1–0) and Lyα lines, observed with the Atacama Large Millimeter Array and Keck telescope, respectively, in the field of the submillimetre-selected galaxy SMM J02399−0136 at z ∼ 2.8, which comprises a heavily obscured starburst galaxy and a broad absorption line quasar, immersed in a large Lyα nebula. This comparison highlights the critical role played by turbulence in channelling the energy across gas phases and scales, splitting the energy trail between hot/thermal and cool/turbulent phases in the circumgalactic medium (CGM). The unique chemical and spectroscopic properties of CH⁺ are used to infer the existence of a massive ($\sim$3.5 × 10^{10} M$_\odot$), highly turbulent reservoir of diffuse molecular gas of radius ∼20 kpc coinciding with the core of the Lyα nebula. The whole cool and cold CGM is shown to be inflowing towards the galaxies at a velocity $\sim$ 400 km s^{-1}. Several kpc-scale shocks are detected tentatively in CH⁺ emission. Their linewidth and specific location in space and velocity with respect to the high-velocity Lyα emission suggest that they lie at the interface of the inflowing CGM and the high-velocity outflowing gas. They signpost the feeding of CGM turbulence by active galactic nuclei- and stellar-driven outflows. The mass and energy budgets of the CGM require net mass accretion at a rate commensurate with the star formation rate. From this similarity, we infer that the merger-driven burst of star formation and black-hole growth are ultimately fuelled by large-scale gas accretion.

Key words: molecular processes – turbulence – galaxies: formation – galaxies: high-redshift – galaxies: intergalactic medium – galaxies: starburst.

1 INTRODUCTION

In cosmological simulations, the growth of galaxies in the early universe results from the accretion of pristine gas in virialized dark matter haloes, modulo ejection of matter by stars and active galactic nuclei (AGNs; e.g. Madau & Dickinson 2014; Schaye et al. 2015; Somerville & Davé 2015; Hopkins et al. 2018; Tacconi, Genzel & Sternberg 2020). This gas regulation involves complex exchanges of mass and energy that take place in the circumgalactic medium (CGM) around growing galaxies. So, the CGM naturally holds many of the clues to the physics of galaxy evolution (Tumlinson, Peeples & Werk 2017; Hafen et al. 2019; Wright et al. 2020). The challenges raised by feedback, and by AGN-driven winds in particular, are so prodigious that they have only started to be touched by new generations of numerical simulations (e.g. Biernacki & Teyssier 2018; Richings &

Faucher-Giguère 2018b; Costa, Pakmor & Springel 2020; Davé et al. 2020).

Observationally, a new era is opening up (see the review by Hodge & da Cunha 2020). While ejection is observed via ubiquitous ionized and neutral galactic winds (e.g. Rupke 2018; Faisst et al. 2020; Veilleux et al. 2020) and contributes to the self-regulation of cosmic star formation, evidence of accretion is slowly building up (Bouché et al. 2013; Schroetter et al. 2019; Zabl et al. 2019; Bielby et al. 2020; Walter et al. 2020; Fu et al. 2021).

One new avenue is the direct detection of extended haloes (∼10 kpc) of [C II] or CO emission around high-redshift galaxies (Ivison et al. 2010b, 2011; Carilli & Walter 2013; Tumlinson et al. 2017), but the dynamics of the gas traced by line emission of extended haloes cannot be unambiguously ascribed to inflows or outflows (see e.g. Fujimoto et al. 2019). Only absorption lines provide the straightforward space-velocity information to disentangle inflows from outflows, without providing the physical origin of inflows, though.

★ E-mail: alba.vidal@ens.fr (AV-G); edith.falgarone@ens.fr (EF)

As bright submillimetre sources, dusty starburst galaxies at high redshift provide unique background sources to probe the environment of growing galaxies using highly sensitive absorption spectroscopy in the submillimetre domain, just as quasars do in the visible domain. The power of absorption spectroscopy is even greater against gravitationally lensed starburst galaxies that allow far more sensitive detections. The submillimetre domain happens to be that of the fundamental transitions of light hydrides that, by linking hydrogen with heavy elements, are the very first steps of chemistry in space (Gerin, Neufeld & Goicoechea 2016). Light hydrides have very high dipole moments so that the critical density of their fundamental transition is orders of magnitude higher than that of CO(1–0), the usual tracer of molecular gas. In diffuse molecular gas, their $J = 1$ level is therefore weakly populated, so that molecular gas of low density ($n_H < 10^3$ cm^{-3}) can be uniquely detected by absorption of the fundamental transition of light hydrides against submillimetre background sources (see e.g. Riechers et al. 2013; Indriolo et al. 2018; Berta et al. 2021, for OH$^+$ lines).

Among all hydrides, CH$^+$, one of the three first molecular species ever detected in space (Douglas & Herzberg 1941), has unique chemical and spectroscopic properties, such that it highlights the sites of dissipation of mechanical energy (Draine 1986; Gredel, van Dishoeck & Black 1993; Federman et al. 1996; Godard, Falgarone & Pineau des Forêts 2009, 2014). Seen in absorption, it reveals not only the presence of low-density molecular gas but also the trails of the suprathermal energy in this medium. Turbulent transport in a biphase medium comprising cold ($T \sim 100$ K) and warm ($T \sim 10^4$ K) neutral phases may also contribute to CH$^+$ production in diffuse gas (Valdivia et al. 2017). In either case, absorption of CH$^+$(1–0) traces the small pockets of 'lukewarm' gas in a cold medium of low density. In the rest of the paper, the term 'cool molecular gas' is adopted for the gas phase seen in CH$^+$(1–0) absorption.[1]

With the Atacama Large Millimeter Array (ALMA), the CH$^+$($J = 1$–0) line has been detected in all the lensed submillimetre-selected galaxies (SMGs) targeted so far at redshifts $z = 1.7$–4.2 (Falgarone et al. 2017, hereafter Paper I; Vidal-Garcia et al. in preparation). Most of these are lensed starburst galaxies discovered by *Herschel* (Eales et al. 2010; Oliver et al. 2010). CH$^+$ absorption lines, found in 15 of the 18 SMGs observed, are unexpectedly deep (opacities 0.25–1.20) and broad [average full width at half-maximum (FWHM) $\sim$400 km s^{-1}]. The emission lines, when fully visible, are extremely broad (FWHM $\sim$1500 km s^{-1}) and are understood as originating in myriad molecular shocks (Godard et al. 2019), presumably powered by hot galactic winds penetrating the CGM (Paper I).

In Paper I, we assumed that the width of the absorption lines is dominated by turbulence and show that the CH$^+$(1–0) absorption lines reveal previously unseen massive and highly turbulent reservoirs (TRs) of diffuse molecular gas ($M_{TR} \sim 10^{10}$ M$_\odot$) extending far outside ($>$10 kpc) the compact starburst cores of radii $\approx$1 kpc. As absorption lines alone cannot provide the extent of the absorbing medium along the line-of-sight, the original method followed to determine the radius (and mass) of the diffuse gas traced by CH$^+$ absorption involves several assumptions (Paper I and Appendix A):

(i) the high occurrence of absorption detections suggests not only that the surface filling factor of the diffuse gas against the background continuum source is high but also that the turbulent reservoirs of diffuse molecular gas and the starburst phase are coeval. We thus assume that the TR lifetime is of the order of the duration of the starburst phase, $t_{SB} \sim 50$–100 Myr (Greve et al. 2005; Tacconi et al. 2008),

(ii) following results obtained in the Milky Way (Godard et al. 2014), the CH$^+$ abundance in this diffuse molecular gas is assumed to be proportional to the turbulent energy transfer rate per unit volume, $\epsilon \sim \overline{\rho}\,\overline{v}_{turb}^3/r_{TR}$, that depends on the average gas mass density $\overline{\rho}$ within the TR volume, on the mean turbulent velocity inferred from the observed absorption line width, $\overline{v}_{turb} = 0.7\Delta v_{abs}$, and on the unknown radius r_{TR}, causing a degeneracy between the CH$^+$ abundance, $X(CH^+)$, and r_{TR},

(iii) we break this degeneracy with the finding that, in the few cases where the stellar mass of the starburst galaxy is known, the radius r_{esc} at which the escape velocity of the galaxy surrounded by its massive CGM is equal to the mean turbulent velocity is such that $r_{esc} \sim \overline{v}_{turb} \times t_{SB}$ within a factor of 2, in spite of stellar masses differing by a factor of 10 and very different gas velocity dispersions. This is why both the TR lifetime and the starburst phase duration, t_{SB}, are about equal to the dynamical time of the TR large-scale turbulence, $t_{dyn} \sim r_{TR}/\overline{v}_{turb}$.

A validation of these unrelated assumptions can only be achieved by direct imaging of the CGM. This was the primary goal of this work, in which we compare our CH$^+$(1–0) absorption results with the Lyα line emission in SMM J02399−0136 at $z \sim 2.8$, previously detected (Ivison et al. 1998; Vernet & Cimatti 2001) and recently imaged at high spectral resolution, $R \approx 4000$, with the Keck/KCWI (Li et al. 2019). As often, this primary goal has been largely exceeded and the Lyα– CH$^+$ comparison in space, and even more importantly in velocity-space, has opened up new perspectives that we also report in this paper.

SMM J02399−0136, the first SMG ever found, is gravitationally lensed by the foreground galaxy cluster Abell 370 with a magnification factor in the range $\mu = 2.0$–3.2[2] (Magnelli et al. 2012; Johnson et al. 2014; Richard et al. 2014; Diego et al. 2016). Its total intrinsic bolometric luminosity is $L_{bol} = 1.2 \times 10^{13}$ L$_\odot$ (Ivison et al. 2010a). It is a complex and vast galactic nursery (see Table 1 and Fig. 1) that harbours the starburst galaxy detected in the FIR dust continuum emission (L2SW), a broad absorption line quasar (BAL QSO) also seen in the FIR continuum (L1) and faint companions visible in the rest-frame UV (L2 and L1N) and undetected in the FIR. A new Lyα emitter, L3, has been recently discovered in the field (Li et al. 2019).

The starburst galaxy provides 58 per cent of the total IR luminosity ($\log_{10} L_{IR} = 12.94 \pm 0.05$, corrected for gravitational amplification – Magnelli et al. 2012), as judged by the relative fractions of rest-frame 122-µm continuum emission from L1 and L2SW in naturally weighted ALMA images (Ferkinhoff et al. 2015). The implied SFR for L2SW is around 870 M$_\odot$ yr^{-1} for a Salpeter (1955) stellar initial mass function (IMF) covering 0.1–100 M$_\odot$ (e.g. Kennicutt 1998), ignoring the considerable uncertainty related to the IMF. The molecular gas mass inferred from CO observations is $M_{H_2} = (2.3 \pm 0.3) \times 10^{11}(\alpha_{CO}/2.1)$ M$_\odot$, where the CO-to-H$_2$ conversion factor is taken to the average $\alpha_{CO} = 2.1$ M$_\odot$ (K km s^{-1} pc^2)$^{-1}$ over its various gas-rich components (Frayer et al. 2018). It extends over

---

[1] We note here that cold for Lyα observers and cosmologists is $T \sim 10^4$ K, while it is $T \sim 10$ K or below for submillimetre astronomers and $T \sim 10^2$ K for radioastronomers, which is the temperature of the cold neutral medium in thermal pressure balance with the warm neutral medium at $T \sim 10^4$ K. The cool molecular gas traced by CH$^+$(1–0) absorption is warmer than the bulk of star-forming molecular clouds at $T \sim 10$–40 K.

[2] Magnification values obtained from the *Hubble Space Telescope* (*HST*) Frontier Fields programme (Lotz et al. 2017) that includes different models of the lens maps for Abell 370 (https://archive.stsci.edu/prepds/frontier/lensmodels/).

Table 1. Known components of SMM J02399−0136.

Name	α_{J2000} (h min s)	δ_{J2000} (° ′ ″)	Description	References
ELAN			Enormous Lyα nebula around the entire system	1, 2
L1	02:39:51.815 [a]	−01:35:58.39	Dusty BAL QSO	1, 3, 5
L1N	02:39:51.838 [c]	−01:35:57.19	Marginally extended and somewhat bluer northern companion to the QSO	1, 4
W1 [d]			Feature extending westwards for several arcsec from BAL QSO, seen in CO(3–2)	5
L2	02:39:52.00 [b]	−01:35:57.5	Low-surface-brightness blue structure, east of BAL QSO	1, 4
L2SW	02:39:51.951 [a]	−01:35:58.92	Highly obscured gas-rich starburst galaxy near BAL QSO	4
L3	02:39:51.59 [b]	−01:36:04.8	Faint Lyα blob	2

Notes. 1 – Ivison et al. (1998); 2 – Li et al. (2019); 3 – Vernet & Cimatti (2001); 4 – Ivison et al. (2010a); 5 – Frayer et al. (2018).
[a]Coordinates for L1 and L2SW are measured from the ALMA continuum imaging of Frayer et al. (2018), accurate to ±0.001 and ±0.002 s in α_{J2000}, respectively, and ±0.02 arcsec in δ_{J2000}. [b]For L2 and L3, the positions come from Li et al. (2019), corrected for the difference between their position for L1 and that of Frayer et al. (2018). [c]For L1N, the position comes from the Abell 370 Frontier Fields *Hubble Space Telescope* imaging of Lotz et al. (2017), corrected for the difference between the position for L1 and that of Frayer et al. (2018). [d]The position of W1 cannot be given accurately because it is an extended and elongated source (see fig. 5 in Frayer et al. 2018).
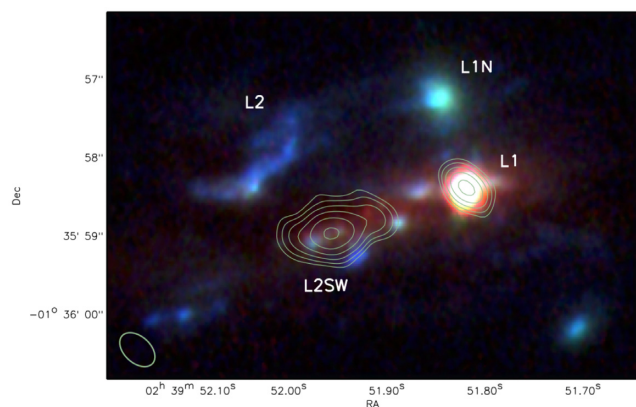

Figure 1. Overview of the galaxy group, SMM J02399−0136. The key components are labelled: L2SW for the dusty starburst and L1 for the BAL QSO, following the notation of Ivison et al. (2010a). ALMA rest-frame 360-μm continuum image with contours starting at 3σ, spaced by $\sqrt{2}$, where the peak is 1.58 mJy beam^{-1} and the local rms noise, σ, is 55 μJy beam^{-1}. The Frontier Fields *HST* frames (Lotz et al. 2017) used to make the underlying false-colour composite were shifted 0.1 arcsec west and 0.1 arcsec south to align with the available *Gaia* stars. The astrometry is then good to better than a small fraction of the ALMA synthesised beam, shown inset. The Lyα blob, L3, is out of the field and the extended CO structure, W1, is not shown.

∼25 kpc in the source plane (Frayer et al. 1998; Ivison et al. 2010a). A new massive elongated structure (W1) extending 13 kpc westwards of L1 has been recently discovered by Frayer et al. (2018). It is detected in CO(1–0) single-dish and ALMA CO(3–2) observations, but undetected in higher J CO lines with ALMA. The nature of this low-excitation component, with a velocity redshifted with respect to that of L1, is undetermined.

For $H_0 = 67.4$ km s^{-1} Mpc^{-1}, $\Omega_{\text{M}} = 0.315$, and $\Omega_\Lambda = 0.685$ (Planck Collaboration VI 2020), 1 arcsec corresponds to a proper size of 8.0 kpc at $z = 2.8$ (uncorrected for lensing magnification which acts mainly east–west, Frayer et al. 2018). Throughout the paper, we adopt a correction of × 2.25 along the shear direction and ×1.06 perpendicular to that, giving a total of ×2.38 (Ivison et al. 2010a). The correspondences 3.55 kpc arcsec^{-1}, 7.55 kpc arcsec^{-1} and 3.36 kpc arcsec^{-1} are therefore used in the east–west, north–south, and NE–SW (and NW–SE) directions, respectively.

The paper is organized as follows: Section 2 is dedicated to the improved determination of the galaxy redshifts, the ALMA and IRAM–30m CH$^+$(1–0) results are presented in Section 3, the summary of the Keck/KCWI Lyα results is given in Section 4, the

comparison of the CH$^+$(1–0) and Lyα data is conducted in Section 5. The discussion, in Section 6, includes the many CO observations of this galaxy group and an estimation of the energy budget. The paper ends in Section 7 with a summary of our findings and open questions.

2 IMPROVED REDSHIFT MEASUREMENTS FOR THE L1 AND L2SW GALAXIES

The redshifts used in the various observations of SMM J02399−0136 are different: $z = 2.803$ in Ivison et al. (1998), Frayer et al. (1998), and the present CH$^+$ observations, $z = 2.808$ in Genzel et al. (2003) and Frayer et al. (2018) and $z = 2.8048$ for the Lyα observations (Li et al. 2019). They correspond to redshift determinations achieved with different lines and angular resolutions. The velocity difference corresponding to the two extreme redshifts is ∼300 km s^{-1}, with a remarkable trend: the larger the beam and the lower the line excitation, the higher the redshift.[3] In this paper, all the velocity scales are computed with respect to a reference redshift $z_{\text{ref}} = 2.8041 \pm 0.0004$ inferred from an ALMA CO(7–6) image at higher resolution (0.48 arcsec × 0.46 arcsec) than that published (0.72 arcsec × 0.61 arcsec) in Frayer et al. (2018), obtained using Briggs weighting rather than natural weighting to maximize the resolution. The CO(7–6) high excitation line is a better tracer of the dense hot starburst cores than the lower excitation CO(3–2) line, even observed at high angular resolution with ALMA: the CO(3–2) channel maps in Frayer et al. (2018) clearly show the existence of an extended low excitation component at $v \sim 340$ km s^{-1} that contaminates the L1 and L2SW line profiles. From the new 1 mm continuum map, the positions of the galaxies, based on the radio phase calibrators, are given in Table 1. In the CO(7–6) line data cube, the centre velocity of the galaxies shifts to the red for larger apertures. For an aperture associated with the beam size, the velocities [on the $z = 2.808$ scale, that of the CO(7-6) ALMA data] of the mid-points of the half-power strengths centred on the 1 mm continuum positions are $v_{\text{L1}} = -297 \pm 30$ km s^{-1} and $v_{\text{L2SW}} = -320 \pm 20$ km s^{-1}. The velocity difference between L1 and L2SW being only 23 km s^{-1}, the reference redshift for the two galaxies, z_{ref}, is inferred from the observed average velocity −308.5 km s^{-1} of the two galaxies in the $z = 2.808$ scale. It provides the best reference frame for the galaxies themselves, because it combines the highest angular resolution with

---

[3]Similarly, two redshifts differing by ∼300 km s^{-1} have been measured for the starburst galaxy G09v1.40 (Bussmann et al. 2013; Yang et al. 2017) likely due to a large-scale outflow detected in CH$^+$ emission (Paper I).
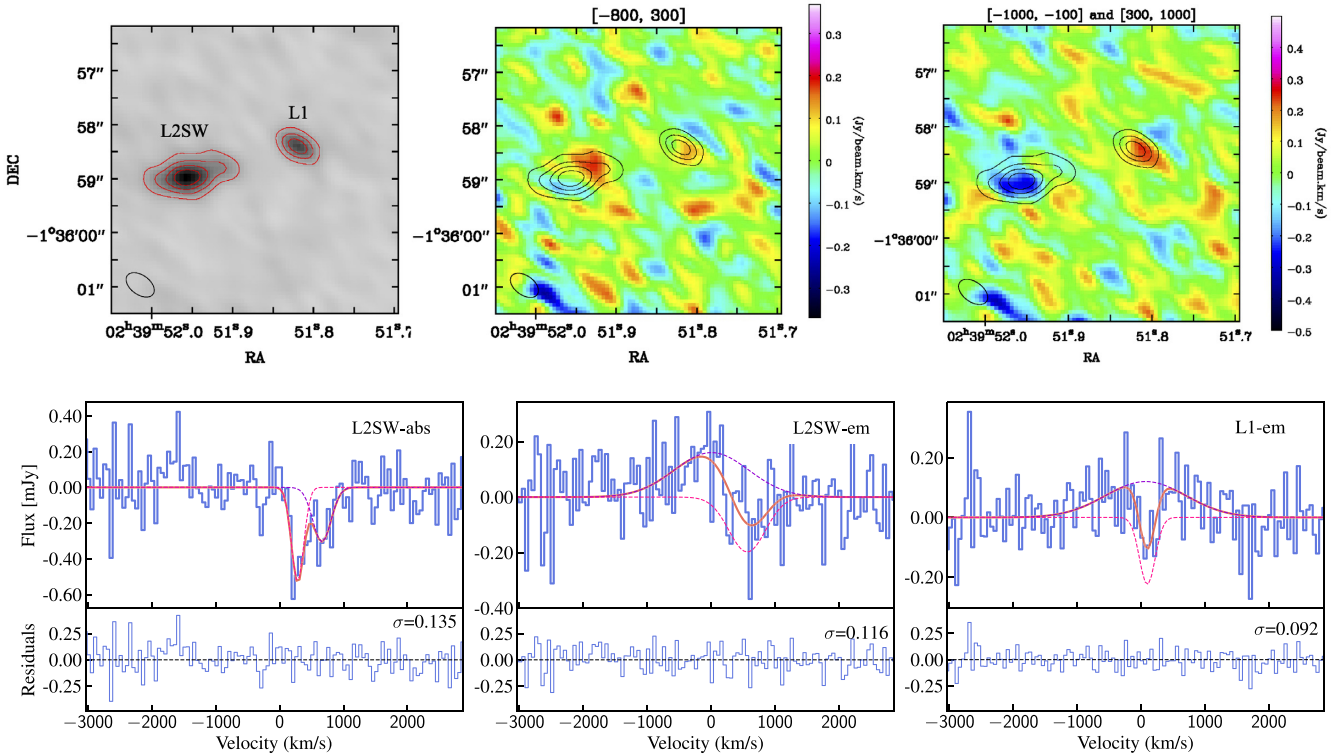
Figure 2. *Upper row (left):* ALMA rest-frame 360-µm continuum image of SMM J02399−0136 (grey scale and red contours at 20, 40, 60, and 80 per cent of the peak at 1.58 mJy beam^{-1}) with $\sigma = 55$ µJy beam^{-1}. The SMG is labelled L2SW and the BAL QSO L1, following the notations of Ivison et al. (2010a). The synthesized beam is shown in the bottom left corner. *(Middle):* Map of the CH$^+$ line integrated area (i.e. moment-0) over the velocity range [−800, 300] km s^{-1}. The rms noise level over the displayed area is $\sigma_{m0} = 0.06$ Jy km s^{-1} beam^{-1}. *(Right):* CH$^+$ moment-0 map over the velocity range [−1000, −100] and [300, 1000] km s^{-1}. The rms noise level over the displayed area is $\sigma_{m0} = 0.08$ Jy km s^{-1} beam^{-1}. The black contours show the dust continuum emission of the galaxies. *Lower row:* Three CH$^+$(1–0) continuum-subtracted ALMA spectra, with Gaussian fits of the emission and absorption. The origin of the velocity scale is at $z_{ref} = 2.8041$. The dashed lines show individual Gaussian components, in absorption and/or emission. The residual spectra and the rms noise level are also displayed. The spectra are obtained over the L2SW extended continuum peak (80 per cent contour level) *(left)*, and over the extended regions at levels $\geq \sigma_{m0}$ (yellow range) ∼0.5 arcsec west of L2SW *(middle)* and extending over ∼1 arcsec south-west of L1 *(right)*.

the kinematics of the CO(7–6) lines that peak at the same positions as the 1 mm continuum sources.

All the velocities reported in the paper are measured in this reference frame. The absolute velocity estimates are uncertain by only ±15 km s^{-1}, corresponding to the uncertainty on z_{ref}.

3 THE CH$^+$(1–0) PERSPECTIVE

3.1 ALMA observations and results

SMM J02399−0136 is one of eight SMGs observed for the first time in ALMA Cycle 4 as part of project 2016.1.00282.S. The CH$^+$(1–0) line [$\nu_{rest} = 835.137$ GHz, Amano (2010)] at redshift $z \sim 2.8$ is shifted into ALMA Band 6 at frequency 219.5 GHz. Observations were done with 42 antennas in configuration C40-4. The minimum and maximum baselines were 15 m and 704 m, respectively, providing a maximum recoverable size of ∼5 arcsec. J0238+1636, J0239−0234, and J0006−0623 were observed as bandpass, phase, and flux calibrators. Data reduction was performed within the Common Astronomy Software Application (CASA) version 5.4.0. We followed the standard ALMA pipeline data reduction. Visual inspection of the different calibration steps, i.e. bandpass, phase, amplitude, and flux, showed satisfactory calibration. We additionally flag antenna DV23 during a short period of time because

of bad amplitude. Imaging was done in the same CASA version. We cleaned the data using the CASA task *tclean*, with the hogbom algorithm. We spectrally regridded the data to a channel width of 50 km s^{-1}. To deconvolve the image, we used a mask contouring the sources which was defined in the continuum image. The restored synthesized beam size is 0.59 arcsec × 0.36 arcsec (PA = 54 deg). The phase centre is RA: 2^{h}39^{m}51^{s}86; Dec: −1°35′58″81 (J2000).

The ALMA rest-frame 360 µm continuum image of SMM J02399−0136 is shown in Figs 1 and 2. Only the starburst galaxy, L2SW, and the BAL QSO, L1, are detected. The radius of the starburst galaxy L2SW in the source plane has been inferred from a simplified lens modelling to be $r_{L2SW} = 1.8 \pm 0.1$ kpc (see Appendix B) consistent with the radii measured for SMGs at redshifts $z \sim 1$–3 for which the mid-IR emission is dominated by star formation (e.g. Ikarashi et al. 2017).

The only three CH$^+$ lines detected in the immediate vicinity of L1 and L2SW are displayed in Fig. 2. In the direction of the L2SW peak of dust continuum emission, only absorption is observed: it is redshifted with respect to the galaxies average velocity. An inverse P-Cygni profile is observed one synthesized beam westwards of this peak. In the direction of L1, there is no absorption detected against the peak continuum emission but the upper limit is high, $\tau_0 < 0.7$, because the continuum source is weak. Absorption is tentatively detected one synthesized beam west of the peak, mostly

Table 2. Characteristics of the CH^+ line profiles and inferred properties of the turbulent reservoir around L2SW and L1, computed for $t_{SB} = 66$ Myr. All the velocities are given with respect to $z_{ref} = 2.8041$.

Source		S^a_{cont} (mJy)	v_{abs} (km s^{-1})	Δv_{abs} (km s^{-1})	v_{em} (km s^{-1})	Δv_{em} (km s^{-1})	τ_0	$N(CH^+)$ (10^{14} cm^{-2})	r_{TR} (kpc)	X(CH^+) (10^{-8})	M_{TR} (10^{10} M$_\odot$)
L2SW	LV[b]	1.5	280 ± 40	210 ± 70	–	–	0.45	2.9		0.7	
	HV[b]		660 ± 70	290 ± 160	–	–	0.26	2.3		1.3	
	LV+HV[c]		430 ± 40	580 ± 100	–	–	0.29	5.0	23	5.2	3.5[d]
L2SW-em		0.7	600 ± 180	750 ± 440	40 ± 380	1280 ± 640	0.37	8.3	30	8.8	4.4[d]
L1-em		0.4	80 ± 90	290 ± 130	60 ± 240	1350 ± 440	0.62	5.4	12	1.3	3.3[e]
Average[f]			380 ± 200	490 ± 470	55 ± 450			6.2	22		3.7

[a]Rest-frame 360 μm continuum flux of the galaxies. [b]Low (LV) and high (HV) velocity components in Fig. 2 (bottom left). [c]Fit with one single component that allows the determination of the global TR properties. [d]Mass estimated for $r_{SMG} = 1.8$ kpc, the intrinsic radius of L2SW inferred from lens modelling (Appendix B). [e]Mass estimated for $r_{SMG} = 0.8$ kpc (Appendix B). [f]Weighted averages for v_{abs}, Δv_{abs}, and v_{em} of the single component fit for L2SW, L2SW-em, and L1-em.

against the CH^+ line emission. The regions over which absorption and emission are detected appear at the $\sim 3\sigma_{m0}$ level in the moment-0 maps of Fig. 2 computed over two different velocity intervals (σ_{m0} is the rms noise level of the moment-0 maps). In L1 and L2SW, the CH^+ emitting regions are more extended, at that level, than the synthesized beam and spatially offset from the continuum peaks, an offset already reported in Paper I for other starburst galaxies.

The line profiles are decomposed into Gaussian components: one or two components in absorption and one in emission. The parameters in Table 2 are inferred from the fits made simultaneously to the emission and absorption lines: Δv_{em} and Δv_{abs} are the FWHM of the emission and absorption lines, v_{abs} (resp. v_{em}) is the offset velocity of the absorption (resp. emission) Gaussian with respect to the redshift $z_{ref} = 2.8041$ (Section 2). The uncertainties on the parameters have not been evaluated with the bootstrap method to take into account the correlation between these parameters because the emission lines are only tentatively detected.

A remarkable feature in the moment-0 maps of Fig. 2 is the presence in the L1 environment of elongated structures above the σ_{m0} level, whose shape depends on the velocity range over which the line moment-0 is computed. To highlight the velocity-dependence of their shape, Fig. 3 displays the overlays of all the extended structures brighter than σ_{m0} in four different moment-0 maps of the close environment of L1 and L2SW. The choice of their velocity coverage optimizes the signal-to-noise ratio of the moment-0 values (i.e. coverage of 1000 and 1600 km s^{-1} much larger than the resolution to increase the signal but not as large as the lines themselves to limit the noise level), while the choice of their velocity reflects the distribution of the structures in velocity. The overlays of extended structures weaker than $-\sigma_{m0}$ in the same moment-0 maps are also shown. CH^+ spectra integrated over areas encompassing the structure contours in the four different moment-0 maps are also displayed in Fig. 3. These structures are possible regions of CH^+ line emission located within ~ 10 kpc from the BAL QSO, L1.

A search for emission lines further away from the galaxies, conducted in velocity-space and space over the 1/3 primary beam of the ALMA observations (43 arcsec/3 $\approx$ 14 arcsec), has led to the discovery of possible additional structures of CH^+ emission. The criteria used to identify structures in different moment-0 maps are: (i) line-integrated intensity brighter than the σ_{m0} level, where σ_{m0} is the rms noise level of the moment-0 values over the searched area, (ii) more extended, at that level, than the synthesized beam, i.e. $\Omega > 0.17$ arcsec^2 and (iii) localized within the 1/3-primary beam area where the noise is minimum (i.e. at a distance less than 7 arcsec from

the phase centre). No lower limit on the linewidth was included in the selection criteria. The search was performed with CASA and is by no means a systematic search of all the CH^+ emission spots. This is the goal of an on-going study (Hayatsu et al. in preparation).

However, the number of negative extended structures challenges the statistical significance of the positive structures. While the number of positive structures exceeds that of negative structures close to the phase centre (Fig. 3), it is less clear cut in the wider field, out to the 1/3 response point of the primary beam (Fig. 4). We show in Appendix C that the bright and extended negative structures could be due to combined sidelobes of multiple regions of weak emission and that the number of pixels in positive extended structures larger than one synthesized beam exceeds that in negative ones within 4.5 arcsec from the centre of phase (Fig. C1). This positive excess suggests that a fraction of the positive structures in the inner part of the ALMA field of view are not due to residual sidelobes, although this excess does not tell which are the real emission structures and which are the sidelobes among the positive ones. We also note that, as the total power is missing in our ALMA data, in particular its spatial distribution over a few arcsec, the power in the structures of negative moment-0 is overestimated.

The CH^+ spectra of seven additional candidates are displayed in Fig. 4 with Gaussian fits to their line profiles and residual spectra. Spectra taken within the same σ_{m0} contour as the selected moment-0 structures but localized in their vicinity are displayed in Fig. C2 to illustrate the high quality of the baselines in the inner part of the ALMA field.

These structures of possible CH^+ line emission are complex because the lines are weak and extremely broad, and emission and absorption coexist over various velocity ranges, depending on the position. This is why, although there are several other prominent positive extended structures in the moment-0 maps of Fig. 4, the seven spectra selected are those for which simultaneous Gaussian fits to the emission and absorption could converge.

The characteristics of these candidate CH^+ emission regions and those in the close vicinity of L1 and L2SW are given in Table 3. The first eight structures are the most plausible because they are located within 4.5 arcsec from the phase centre and the rms noise level of their residuals is <0.2 mJy. The others are less plausible, being further from the phase centre, with noisier spectra but the comparison of their CH^+ emission to that of Lyα suggests that three of them may be real (see Section 5). Note that, although the peak intensity is of the order of the rms noise level in 50 km s^{-1} channels, the signal-to-noise ratios computed over their full linewidth are all ~ 3 because they are extremely broad ($\overline{\Delta v_{em}} \sim 1300$ km s^{-1}).
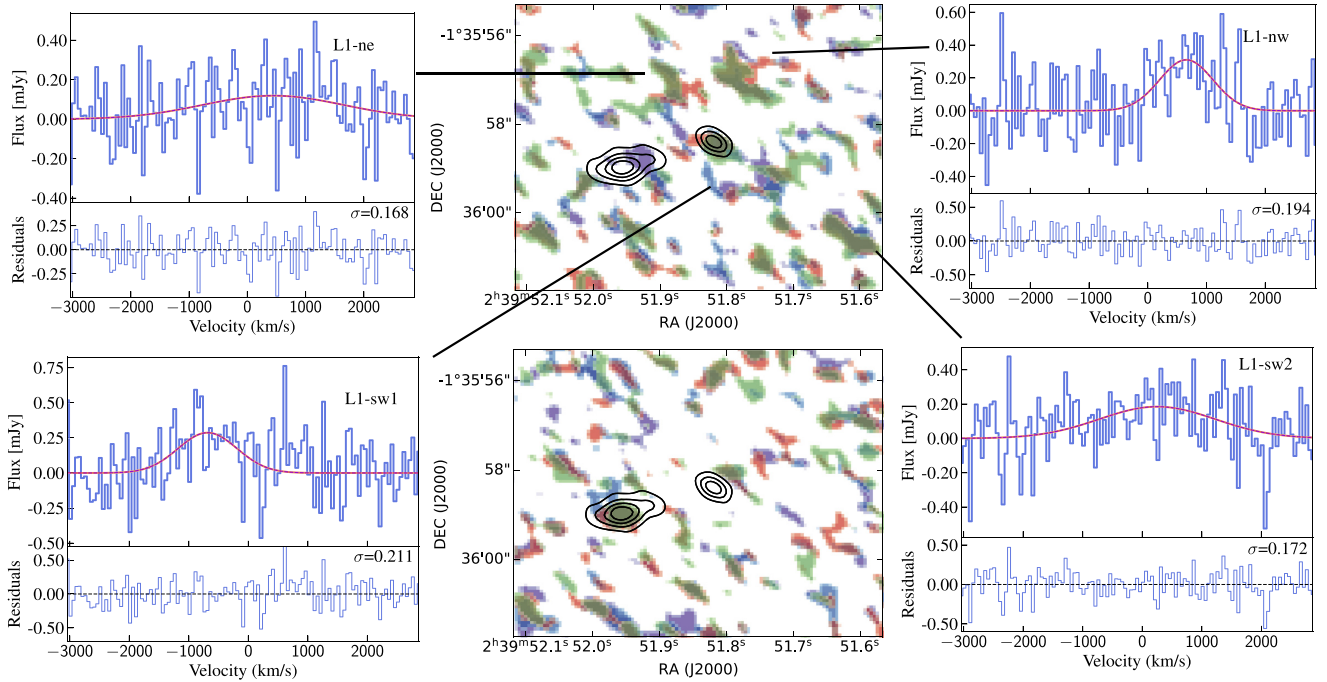
Figure 3. *Central panels:* Overlay of four CH$^+$ moment-0 maps displaying only the pixels brighter than σ_{m0} (*top*) and weaker than $-\sigma_{m0}$ (*bottom*). The velocity coverages of the four moment-0 maps are: $[-1350, 250]$ km s^{-1} (purple), $[-1000, -100]$ and $[300, 1000]$ km s^{-1} (blue), $[0, 1000]$ km s^{-1} (red) and $[500, 1500]$ km s^{-1} (green). The rms noise level over the displayed area are $\sigma_{m0} = 0.06$ and 0.08 Jy km s^{-1} beam^{-1} for the narrower (1000 km s^{-1}) and broader (1600 km s^{-1}) velocity coverage, respectively. *Outer panels:* Four CH$^+$(1–0) continuum-subtracted ALMA spectra of the indicated extended areas encompassing the structure shapes in the different moment-0 maps. Gaussian fits of the emission lines and residual spectra are displayed. The origin of the velocity scale is at $z_{ref} = 2.8041$. The black contours mark the continuum emission of L1 and L2SW, as in Fig. 2.

Four straightforward results regarding the lines of the eight most plausible candidates appear in this table:

(i) their average centroid velocity, $\overline{v}_{em} = 170$ km s^{-1}, is redshifted with respect to the reference frame of the galaxies,

(ii) their centroid velocities are highly scattered, with a standard deviation $\sigma_{v_{em}} = 540$ km s^{-1},

(iii) their average FWHM, $\overline{\Delta v}_{em} = 1330$ km s^{-1}, is extremely large for molecular lines, with FWHM up to ~ 3000 km s^{-1} and their standard deviation is small,

(iv) on average, they are $\sim 3 \times$ more extended than the ALMA synthesized beam area, mostly because of their elongation.

Several of these structures are elongated over more than 1 arcsec, along directions that are not aligned with the lensing shear direction, roughly aligned with the L2SW–L1 direction (Frayer et al. 2018). In a few cases, they are barely resolved in the transverse direction.

3.2 IRAM-30m observations

The CH$^+$(1–0) observations were carried out in June and November 2019 at the frequency $\nu = 219.584$ GHz corresponding to the rest-frame frequency $\nu_0 = 835.079$ GHz of the CH$^+$($J = 1$–0) transition[4] at redshift $z = 2.803$. Two EMIR receivers (Carter et al. 2012) were operated, E0 at 90.9 GHz for the ^{12}CO($J = 3$–2) line and E2 for

the CH$^+$ line. The wobbler was operating at 0.5 Hz with a throw of ± 30 arcsec. The weather conditions were good with a SSB system temperature varying between 160 and 220 K. At this frequency, the half-power beamwidth is 11.2 arcsec (close to the 1/3 ALMA primary beam) and the flux/brightness conversion for point sources is $S[\text{Jy}] = 9.6 \, T_A^*[\text{K}]$. A spectral resolution of 64 MHz provided a velocity resolution of 87 km s^{-1}. The spectra were reduced and analysed with the CLASS package of the GILDAS software.[5]

A broad CH$^+$ line has been tentatively detected with a peak intensity $T_A^* = 0.3 \pm 0.1$ mK in resolution elements of 87 km s^{-1}, a centroid velocity $v_{\text{CH}^+(1-0)} = 100 \pm 170$ km s^{-1}, and an FWHM $\Delta v_{\text{CH}^+(1-0)} = 1300 \pm 500$ km s^{-1} (Fig. 5). The ^{12}CO(3–2) line, $T_A^* = 0.8 \pm 0.2$ mK, is centred at $v_{\text{CO}(3-2)} = 210 \pm 60$ km s^{-1}, and narrower, $\Delta v_{\text{CO}(3-2)} = 800 \pm 100$ km s^{-1}, than the CH$^+$ line (Fig. 5). The offset velocities of the two lines with respect to z_{ref} are similar within the error bars.

The sum of the eight most plausible CH$^+$ line fluxes identified in the ALMA data (Table 3), weighted by the IRAM-30m beam profile at the relevant location, is shown in Fig. 6 (top). This sum is smaller than the flux measured with the single-dish IRAM-30m telescope (Fig. 6, bottom). The line integrated fluxes over $[-1000, 1000]$ km s^{-1} are 1.4 ± 0.4 and 3.5 ± 1.4 Jy km s^{-1} for ALMA and IRAM-30m, respectively. Over a broader interval, $[-1900, 2200]$ km s^{-1}, these integrated fluxes are 2.2 ± 0.5 Jy km s^{-1} and 4.7 ± 1.6 Jy km s^{-1}, indicating that the ensemble of scattered CH$^+$ emission structures detected by ALMA in the inner 4.5 arcsec of the

---

[4]This value is the first to have been determined experimentally by Pearson & Drouin (2006). It differs by only 58.5 MHz, or 21 km s^{-1} from that determined later by Amano (2010).
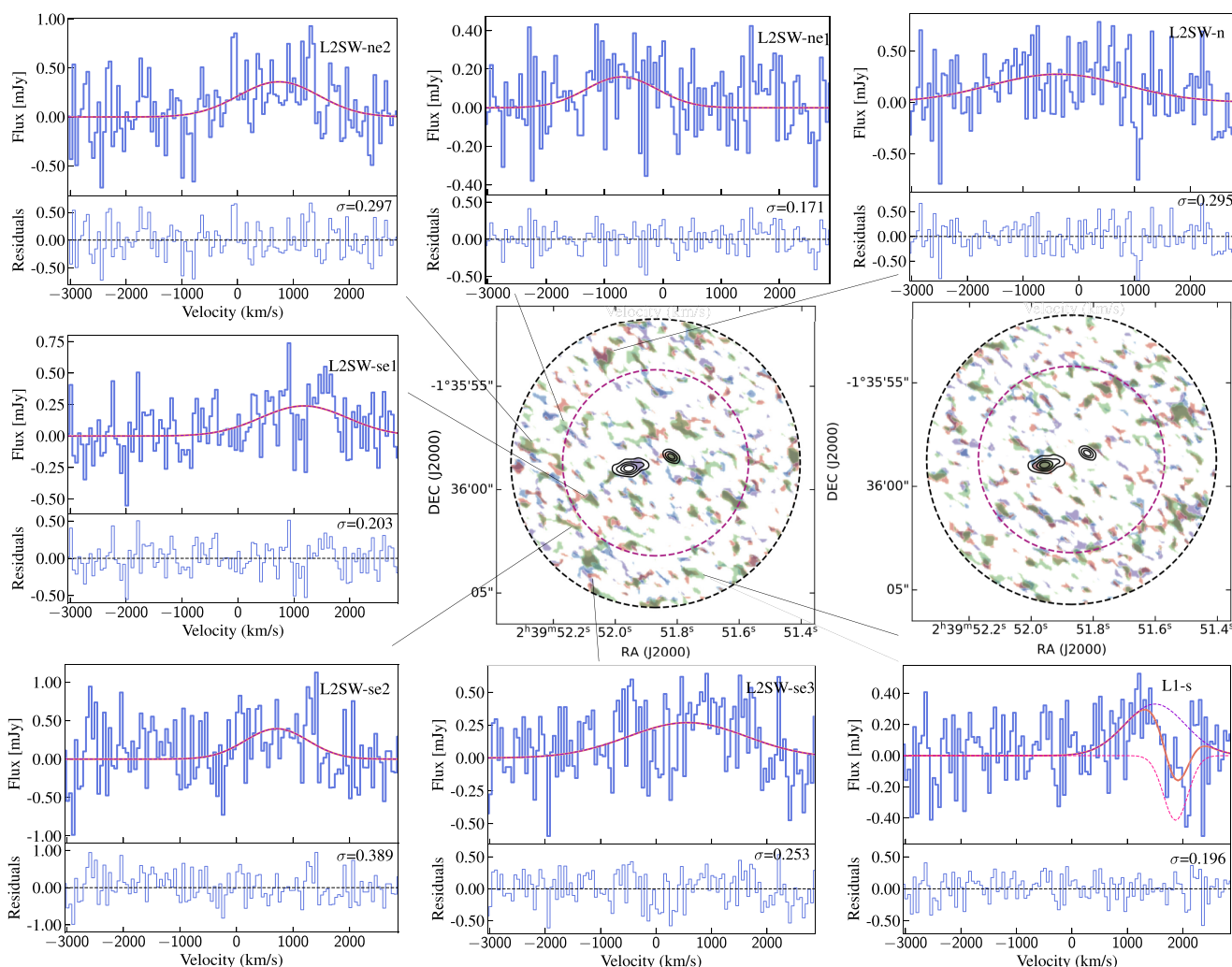
[5]http://www.iram.fr/IRAMFR/GILDAS

Figure 4. Same as Fig. 3 over 1/3 of the ALMA primary beam, shown as a dashed black circle. The rms noise levels of the four moment-0 maps over the 1/3 primary beam of ALMA are similar to those in the field of Fig. 3. The distance of 4.5 arcsec to the phase centre is given by the dashed magenta circle.

field of view contributes to about 50 per cent of the power detected by IRAM-30m.

This comparison suggests that these eight structures are the brightest of a broad distribution of weaker structures that contribute to the single-dish detection but are resolved out by ALMA and/or too weak to be detected. This is also in line with our statement that the CH+ emission structures we report are not a complete census of the CH+ emission spots in the data set. The line shapes of the two spectra in Fig. 6 are notably different, which is likely due to the combination of a complex radiative transfer of the CH+ line (i.e. locally the profiles are P-Cygni and inverse P-Cygni) and ALMA filtering.

Last, we note that the total power detected by the IRAM single-dish telescope, $3.5 \, \mathrm{Jy \, km \, s^{-1}}$ over $2000 \, \mathrm{km \, s^{-1}}$ would correspond, if distributed uniformly, to an integrated line brightness of 4.7 $\mathrm{mJy \, km \, s^{-1} \, beam^{-1}}$ in an ALMA moment-0 map at the resolution $0.59 \, \mathrm{arcsec} \times 0.36 \, \mathrm{arcsec}$, integrated over $1600 \, \mathrm{km \, s^{-1}}$. With a surface filling factor of 8 per cent in the ALMA one-third primary beam, it would amount to $\sim 60 \, \mathrm{mJy \, km \, s^{-1} \, beam^{-1}}$ that is the σ_{m0} level of the moment-0 maps. Recovering the total power and its spatial distribution at a few arcsec scale would possibly shift the moment-0 brightness distributions towards more positive values.

3.3 Properties of the turbulent CGM inferred from the CH+ lines

3.3.1 The CH+ absorption lines

The absorption line optical depth, computed at the velocity v_{abs} of the deepest absorption, is derived from the Gaussian fits:

$$\tau_0 = -\ln \frac{S(v_{\mathrm{abs}})}{S_{\mathrm{cont}} + S_{\mathrm{em}}(v_{\mathrm{abs}})}, \tag{1}$$

with S_{cont} and $S_{\mathrm{em}}(v_{\mathrm{abs}})$ are the dust continuum flux and the line emission flux at velocity v_{abs}, respectively, and $S(v_{\mathrm{abs}})$ is the flux resulting from the absorption. The optical depth estimates of the absorption lines (Table 2) are not affected by differential lensing because the background dust emission photons and those – at the same frequency – that escaped absorption by CH+ molecules have experienced the same lensing. The velocity resolution is coarse and we cannot rule out the possibility that portions of the line might be saturated. The estimated values of $N(\mathrm{CH}^+)$ could therefore be lower limits, so in Table 2 we provide them without a compiled error. However, the rms uncertainty on τ_0 in the spectra of Fig. 2 is ~ 0.15 so that the relative uncertainty on τ_0 is between 25 and 40 per cent.

Table 3. Characteristics of the tentative CH$^+$ emission detections.

Name	Flux density (mJy)	σ^a (mJy)	$v_{em}{}^b$ (km s^{-1})	$\Delta v_{em}{}^b$ (km s^{-1})	S/N^c	d^d (arcsec)	d^e (kpc)	Ω^f (arcsec)^2
L1-em	0.12 ± 0.05	0.09	60 ± 240	1350 ± 440	2.8	1.1	3.9	0.34
L2SW-em	0.16 ± 0.12	0.12	40 ± 380	1280 ± 640	3.0	1.1	3.9	0.38
L1-ne	0.12 ± 0.11	0.17	530 ± 1200	2900 ± 3100	2.7	1.7	5.7	0.46
L1-nw	0.31 ± 0.17	0.19	740 ± 290	1070 ± 690	3.8	2.5	8.4	0.42
L1-sw1	0.29 ± 0.17	0.21	− 600 ± 330	1160 ± 775	3.3	2.0	6.7	1.03
L1-sw2	0.18 ± 0.11	0.17	340 ± 720	2290 ± 1700	3.6	4.5	15.1	0.32
L2SW-ne1	0.16 ± 0.15	0.17	− 620 ± 655	1420 ± 1540	2.5	3.8	12.8	0.44
L2SW-se1	0.24 ± 0.13	0.20	1270 ± 500	1820 ± 1210	3.6	3.2	10.8	0.54
Average	0.25	–	170 ± 540^g	1330 ± 270^g	–		8.4	0.49
L1-s^h	0.34 ± 0.24	0.20	1590 ± 766	1275 ± 940	2.8	5.6	42.3	0.48
L2SW-n	0.27 ± 0.15	0.30	− 285 ± 545	2860 ± 1315	3.4	5.4	25.4	1.85
L2SW-ne2	0.36 ± 0.13	0.30	825 ± 320	1700 ± 750	3.5	5.0	17.8	1.03
L2SW-se2	0.48 ± 0.15	0.40	805 ± 215	1390 ± 500	3.2	5.0	16.8	0.67
L2SW-se3	0.27 ± 0.11	0.25	655 ± 525	2510 ± 1270	3.8	5.3	17.8	1.00
Average^i	0.25	–	412 ± 550^g	1450 ± 390^g	–		28.8	0.75

Note. ^{a}Spectrum noise computed for a spectral resolution $\delta v = 50$ km s^{-1}; ^{b}line centroid and FWHM inferred from the Gaussian fits shown in Figs 3 and 4; ^{c}line signal-to-noise ratio computed over the FWHM; ^{d}projected distance of the structure from the phase centre, expressed in arcsec; ^{e}same distance, expressed in kpc, corrected from lensing shear by adopting the three kpc arcsec^{-1} correspondences in the source plane discussed in Section 1; ^{f}solid angle of the structure, to be compared to the ALMA synthesized beam area, 0.17 arcsec^2; ^{g}weighted averages; ^{h}for this source, absorption was fitted simultaneously with the emission. The absorption parameters are the line centroid $v_{abs} = 1955 \pm 210$ km s^{-1} and FWHM $\Delta v_{abs} = 520 \pm 675$ km s^{-1}, ^{i}Average values for the 13 structures.
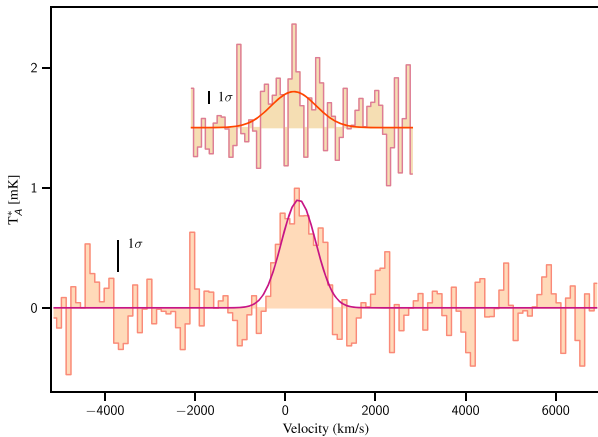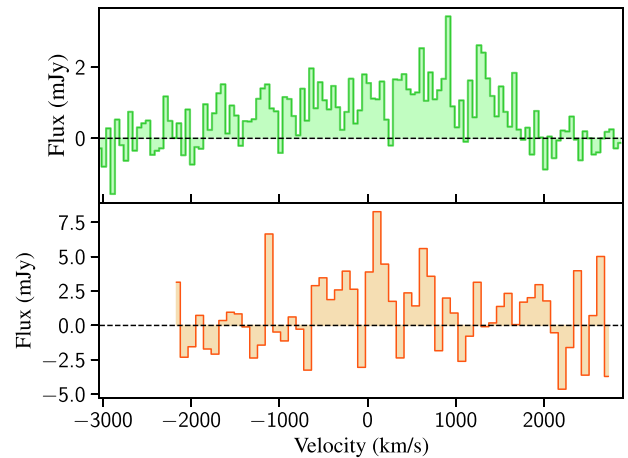

Figure 5. IRAM-30m observations: the CH$^+$(1–0) line (top) and ^{12}CO(3–2) line (bottom) and their Gaussian fits. The origin of the velocity scale is z_{ref} = 2.8041.

Figure 6. Comparison of the sum of all the CH$^+$ emission-line spectra detected by ALMA (top) with the tentative IRAM-30m detection (bottom). The origin of the velocity scale is z_{ref} = 2.8041.

The CH$^+$ column densities are the average values in a solid angle subtended by the area, πr_{SMG}^2, of the background source assumed to be uniformly covered by the absorbing screen:

$$N(CH^+) = 3 \times 10^{12} \text{ cm}^{-2} \, \tau_0 \, (\Delta v_{abs}/1 \text{ km s}^{-1}). \qquad (2)$$

The absorption lines in the direction of L2SW are *redshifted with respect to the galaxies systemic velocity* at $z_{ref} = 2.8041$. These redshifted absorption lines are evidence of several inflowing gas streams on to the SMG at velocities, $v_{in} = v_{abs}$. The projected inflow velocities in the direction of L2SW are large, $v_{in,L2SW} = 280-660$ km s^{-1} (see Table 2). In the direction of L1, the absorption is also redshifted but the offset velocity is much smaller, $v_{in,L1} \sim 80$ km s^{-1}.

Following Paper I, we estimate the radius of the reservoir of diffuse molecular gas at the origin of the CH$^+$ absorption by connecting the CH$^+$ formation rate with the turbulent dissipation rate, assuming that the turbulent dynamical time $r_{TR}/\overline{v}_{turb,TR}$ is of the order of the duration of the starburst phase t_{SB}:

$$r_{TR} = \overline{v}_{turb,TR} t_{SB}. \qquad (3)$$

where $\overline{v}_{turb,TR} = 340$ km s^{-1} is the mean turbulent velocity provided by the weighted-average width of the absorption lines $\overline{v}_{turb,TR} = 0.7 \overline{\Delta v_{abs}}$ (Table 2).

The starburst phase duration, t_{SB}, is often estimated as the consumption time of the molecular gas mass due to star formation, $t_{SB} = M_{H_2}/SFR$. Values of t_{SB} consistent with those of Tacconi et al. (2008), usually around 50–100 Myr, have appeared in the literature as far back as Frayer et al. (1999) and Greve et al. (2005). In the case of SMM J02399−0136, the starburst galaxy itself, L2SW, comprises approximately 25 per cent of the total molecular gas mass (see Frayer et al. 2018) yielding a bespoke value of $t_{SB} \approx 66$ Myr for its SFR of about 870 M$_\odot$ yr^{-1} (Section 1). We caution here that

t_{SB} uncertainties stated in the literature have usually ignored the considerable systematics related to gas mass and SFR – those due to α_{CO} and the IMF, for example.

We recall in Appendix A the method followed to infer the CH$^+$ abundance from the fact that the CH$^+$ formation in the diffuse component is primarily driven by turbulent dissipation. Once r_{TR} is known, the degeneracy between the radius and the CH$^+$ abundance is broken and the mass of the diffuse molecular CGM (TR) can be determined.

In Table 2, the different values of the radius r_{TR}, abundance X(CH$^+$) and mass M_{TR} of the turbulent reservoir obviously refer to the same entity, probed by different sight lines. They are close to each other because the absorption optical depths are similar, being bracketed by unity on the upper side and $\sim$0.2, the sensitivity of the observations on the brightest continuum source. The dynamic range on M_{TR} is therefore limited. The values in Table 2 are computed for $t_{SB} = 66$ Myr, a molecular fraction $f_{H_2} = 1$ and the local density of the absorbing medium, $n_H = 50$ cm^{-3}. This value of the local density is inferred from the Milky Way studies (Godard et al. 2009). An upper limit on the local gas density of $n_H \lesssim 10^3$ cm^{-3} is provided by the fact that the CH$^+$ line is seen in absorption (see Appendix D).

The last line of Table 2 gives the average values of the three estimates of the TR properties derived from the three lines of sight towards L2SW, L2SW-em, and L1-em. The average of the absorption offset velocities, v_{abs}, provides a mean inflow velocity, $\overline{v}_{in} = 380 \pm 200$ km s^{-1} with respect to L1 and L2SW at $z_{ref} = 2.8041$.

The CH$^+$ absorption lines in SMM J02399$-$0136 therefore highlight the presence of a massive turbulent reservoir of diffuse molecular gas, $M_{TR} = 3.7 \times 10^{10} t_{66}^2$ M$_\odot$, where $t_{66} = t_{SB}(66\mathrm{Myr})^{-1}$, inflowing towards the galaxies at $\overline{v}_{in} = 380$ km s^{-1}, a velocity comparable to its mean turbulent velocity $\overline{v}_{turb,TR} = 340$ km s^{-1}. Its inferred radius $r_{TR} \sim 22 t_{66}$ kpc is independent of the lensing magnification, since it is inferred from absorption lines.

3.3.2 The CH$^+$ *emission lines*

The detected line flux densities (Table 3) correspond to line brightness temperatures $\sim$10 mK in the source frame, assuming a uniform brightness over the structure solid angle (see Appendix D). This assumption provides a lower limit for the density in the gas component of the CGM where CH$^+$ is formed and radiates. In Appendix D, we give the results of non-LTE radiative transfer for the CH$^+$($J = 1$–0) emission using the RADEX code (van der Tak et al. 2007). They provide the gas density and temperature conditions required to form a 10 mK emission line, for two relevant CH$^+$ column densities and a local velocity dispersion of 20 km s^{-1}. Densities $n_H \gtrsim 10^4$ cm^{-3} are required for temperatures $<10^4$K and N(CH$^+$) $= 10^{13}$ cm^{-2}.

As the CH$^+$ radical has an extremely short lifetime, $t_{CH^+} \sim 1$ yr (Appendix A), these structures, rich in CH$^+$ and located at distances of several $\times$ 10 kpc from the galaxies, cannot have been stripped by galactic winds from the galaxies' interstellar medium, because the advection time, even at velocities $\sim$1000 km s^{-1} would be >10 Myr. Therefore, CH$^+$ must have formed *in situ*, where it is observed. Given the large CH$^+$ linewidths and the large densities required for line emission, the CH$^+$ seen in emission most likely formed in shocks. However, the CH$^+$ emission lines are extremely broad, with an average FWHM $\sim$1330 km s^{-1} (Table 3), as in several other SMGs (Paper I). CH$^+$ cannot originate in shocks at such high velocities since this would dissociate the H$_2$ molecule needed for the CH$^+$ formation and sputter dust grains necessary for the re-formation of

H$_2$. Most likely they originate in lower velocity ($v_{sh} \approx 20$ km s^{-1}) UV-irradiated molecular shocks (Paper I and Godard et al. 2019). A particularly interesting result of Godard et al. (2019) is that the CH$^+$ column density in the post-shocked layer of these irradiated shocks increases linearly with the UV-field irradiation over a broad range of pre-shock densities.

The large velocity dispersion of the ensemble of individual low-velocity molecular shocks (LVMS) is at the origin of the broad CH$^+$ linewidths. We ascribe it to turbulence generated in the post-shock layer of high-velocity shocks (HVS) in the CGM (see Section 6.2). The dynamical energy transfer between HVS and LVMS might be similar to that observed in the 50-kpc long shock in the Stephan's Quintet driven by a galaxy collision with a gas tidal stream. Within this large-scale shock, the [C II] and CO line velocity dispersions are $\sim$1000 km s^{-1} (Guillard et al. 2012; Appleton et al. 2013, 2017) spanning the velocity difference between the intruder galaxy and the tidal stream of atomic gas.

The physics of such powerful energy transfers between $\sim$10 kpc-scale shocks feeding a turbulent cascade in the multiphase post-shock layers is complex. It is the focus of several recent thorough investigations (e.g. Gaspari, Ruszkowski & Oh 2013; Gaspari, Temi & Brighenti 2017; Gronke & Oh 2020; Li et al. 2020; Lochhaas et al. 2020; Voit et al. 2020).

We show below the added value of a joint investigation of CH$^+$ molecular lines and Lyα observations in this field.

4 THE LYα PERSPECTIVE

SMM J02399$-$0136 was known from the earliest spectroscopic observations with CFHT to be a Lyα emitter and the total extent of the emission was found to be 13 arcsec or $\sim$100 kpc (Ivison et al. 1998; Vernet & Cimatti 2001). These galaxies have recently been observed with the Keck/KCWI (Li et al. 2019) and an extended Lyα nebula has been imaged over $\sim$80 kpc (Fig. 7). However, it is not quite as large and luminous as the Lyα nebulae referred to as ELANe by Cai et al. (2017) and Arrigoni Battaia et al. (2018). The bright-spot, L3, previously unknown, is the focus of Li et al. (2019) who propose that it is a dark cloud made visible by fluorescence excited by the BAL QSO, L1. The spectra observed at the position of the starburst galaxy L2SW, the BAL QSO L1, the blue companion L2, and the dark cloud L3 are shown in Fig. 8. The lines are highly non-Gaussian and asymmetrical close to the QSO. Towards L3, the line is narrow (FWHM = 353 km s^{-1}) and close to Gaussian (Li et al. 2019). Two narrow absorption troughs at $v \sim 150$ and -550 km s^{-1} are also detected at the three positions L1, L2, L2SW and at the same velocities (Fig. 8).

The position–velocity diagram (Fig. 9) shows that the extremely broad Lyα lines (FWZI possibly larger than $\sim$6000 km s^{-1}) are found only in the inner part of the nebula, indeed unresolved by the KCWI observations which had a seeing of 1.5 arcsec (Li et al. 2019), i.e. the extent of the extremely broad Lyα emission in the position–velocity cut.

In its more extended part, the lines are narrower and redshifted with respect to $z_{ref} = 2.8041$ by up to $\sim$750 km s^{-1}. Remarkably, the average velocity across the southern part of the nebula does not change much. At first sight, the Lyα lines cannot be interpreted simply in terms of outflows and inflows, as discussed in Verhamme, Schaerer & Maselli (2006) and Dijkstra (2017) except for the line in the direction of L1 that has a redshifted centroid velocity, computed as its first moment, $C_{1,Ly\alpha} = 260 \pm 40$ km s^{-1}. This redshifted velocity centroid can be seen as a signature of outflowing gas due to the
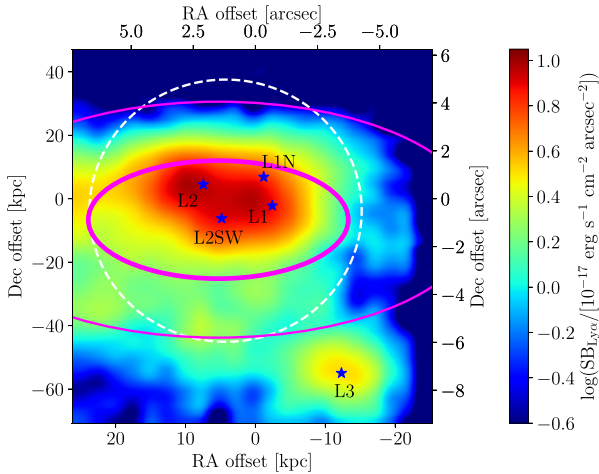
Figure 7. Continuum-subtracted Lyα emission of the gas surrounding SMM J02399−0136 adapted from Li et al. (2019). Note that we have taken the lensing shear direction into account, so that the kpc arcsec⁻¹ correspondence is not the same along the RA and Dec. axis (see Section 1). The magenta ellipses therefore show the size of the turbulent reservoir of diffuse molecular gas seen in CH⁺(1–0) absorption against the L2SW and L1, estimated following the argument of Paper I for $t_{SB} = 50$ Myr (thick) and 100 Myr (thin) that bracket the 66 Myr value found for SMM J02399−0136. The dashed white circle shows the HPBW = 11.2 arcsec of the IRAM-30m telescope at 220 GHz centred at RA (2000) = 02:39:51.89, Dec (2000) = −01:35:58.9.

strong scattering of Lyα photons. However, an infalling CGM could contribute to the blue peak asymmetry as seen in the direction of L2 and to a lesser extent towards L1 and L2SW. The Lyα lines therefore bear the signatures of both outflows and inflows. We show in the next section the unique power of combining CH⁺ and Lyα spectroscopy to get some insight into the CGM gas dynamics on a 50 kpc scale.

5 COMPARISON OF THE CH⁺(1–0) AND LYα PERSPECTIVES

Despite the vast differences between the gas phases emitting and absorbing the CH⁺(1–0) and Lyα lines, a number of straightforward and remarkable properties can be inferred from their comparison.

5.1 The CH⁺ absorptions and Lyα asymmetric line shape

5.1.1 Radius of the halo of diffuse molecular gas

The radius inferred for the turbulent reservoir (TR) of diffuse molecular gas traced by CH⁺(1–0) absorption depends linearly on the duration of the starburst phase (equation 3). This radius is drawn on Fig. 7 for two different values $t_{SB} = 50$ Myr and 100 Myr that bracket the value 66 Myr computed for SMM J02399−0136 (Section 4) and correspond to the range inferred from the statistical studies of SMGs (e.g. Tacconi et al. 2008). These time-scales are uncertain, partly because of the unknown IMF in starburst galaxies (Zhang et al. 2018). However, the broad agreement between the projected extent of the bright core of the Lyα nebula and that of the TR is remarkable. This agreement suggests that the CGM is (at least) biphase with a cool molecular phase of low density ($n_H < 10^3$ cm⁻³) and $T \sim 10^2$ K contributing $\sim 3.5 \times 10^{10}$ M$_\odot$ (Table 2). The warm phase at $T \sim 10^4$ K, the Lyα emitter, is possibly fully ionized.
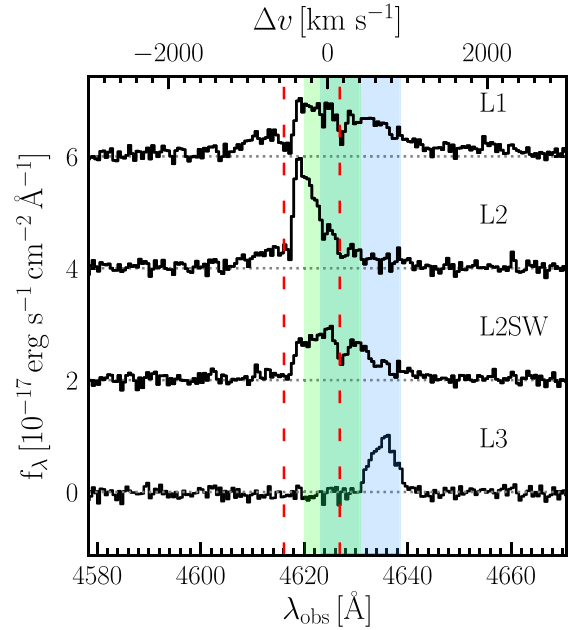

Figure 8. Lyα spectra observed in the direction of L1, L2, L2SW, and L3 by Li et al. (2019). The origin of the velocity scale, computed for $z_{ref} = 2.8041$. The velocity range highlighted in blue (resp. green) is that of the full velocity coverage of the absorption in the direction of L2SW (resp. in the west of L1). Note that the two velocity ranges overlap. The dashed red lines show the uniformity across the field of the velocities of the narrow Lyα absorption troughs at $v \sim -550$ and ~ 150 km s⁻¹. Adapted from Li et al. (2019).

Even more significant, this agreement supports the theoretical basis of our size determination of a CH⁺ absorbing medium, relying on the turbulent dissipation rate and its scaling with size (Paper I). Indeed, this was the original motivation for imaging the Lyα emission of SMM J02399−0136 with the Keck/KCWI.

5.1.2 Inflow signatures

The range of velocities covered by the CH⁺ absorption lines against L2SW and L1 is highlighted in blue and green, respectively, in Fig. 8. All velocities have been computed with respect to $z_{ref} = 2.8041$. Together they cover most of the red side of the Lyα line. As the CH⁺ absorption is redshifted, the cool molecular gas is inflowing towards the galaxies and is located between the galaxies and the observer. This diffuse molecular gas necessarily contains a fraction of atomic hydrogen susceptible to absorb and scatter Lyα photons, most likely at the origin of the Lyα line asymmetry at the three positions, L1, L2, and L2SW.

This same velocity range is also highlighted in blue and green in the position–velocity cut-off (Fig. 9). It is very similar to that of the whole southern part of the Lyα nebula, to which L3 belongs. Unless it is an unlikely coincidence, this means that the bulk of the imaged Lyα nebula is inflowing towards the galaxies because its velocity (and velocity dispersion) is the same as that of the gas causing the redshifted CH⁺(1–0) absorption. This redshifted gas, inflowing towards the galaxies, scatters the Lyα photons back towards the galaxies, and contributes to the weakening of the observed red side of the Lyα line.

Remarkably, the Lyα absorption trough at $v \sim 150$ km s⁻¹ falls at the same velocity as the CH⁺ absorption common to both L1 and L2SW sight lines (Fig. 8). It thus likely corresponds to inflowing

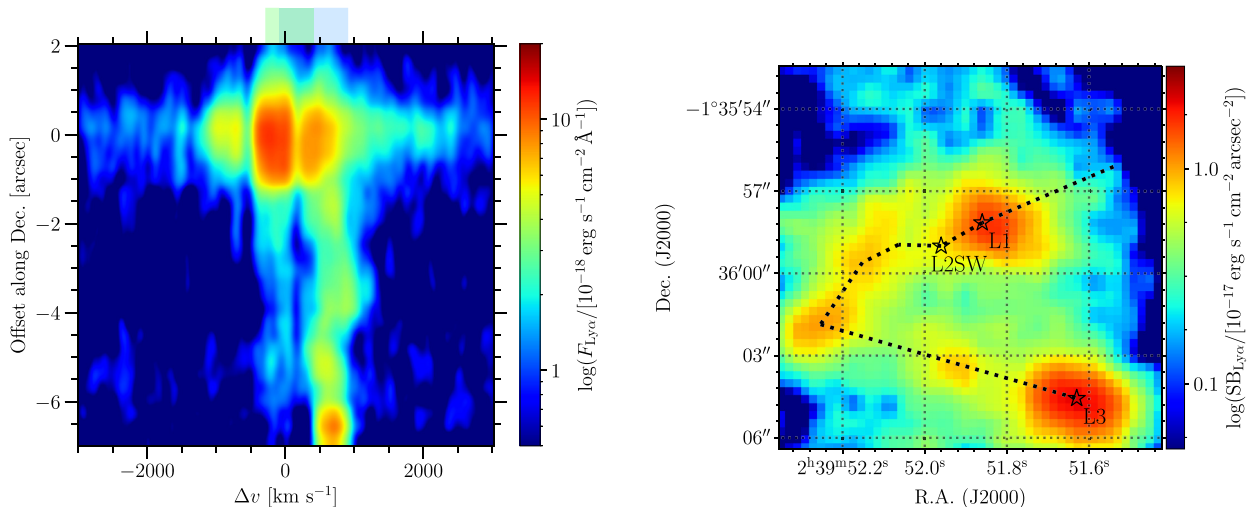**Figure 9.** *Left:* Position–velocity map of the Lyα nebula taken along the track shown in the right-hand panel (black dots). The origin of the velocity scale is $z_{ref} = 2.8041$. The positions are labelled by their offset in declination with respect to L1. Note that the extremely broad Lyα wings, visible from -3000 to $+3000 \, \mathrm{km \, s^{-1}}$ at the position of the BAL QSO L1 are unresolved by the Keck/KCWI observations because of the seeing. The blue and green boxes at the top show the full velocity coverage of the CH$^+$ absorption lines in front of L2SW and L1, respectively, as in Fig. 8. *Right:* Another map of the continuum-subtracted Lyα emission of the gas surrounding SMM J02399−0136 from Li et al. (2019) as Fig. 7, on which the positions used for the position–velocity plot of the left-hand panel are shown. The width of the band used to make this map is narrower than that used in Fig. 7 (5 Å over 4630–4635 Å instead of 30 Å), therefore encompassing only the redder wing of the Lyα line.

gas located between the SMGs and the observer. The other narrow Lyα absorption at $v \sim -550 \, \mathrm{km \, s^{-1}}$ does not coincide with any CH$^+$ absorption trough: it might be caused by gas located *behind* the SMGs, and therefore also inflowing towards the galaxies, but we cannot rule out that it is CH$^+$-poor because metal-poor, reflecting inhomogeneities in the metallicity of inflowing matter. In the former case, since the $-550 \, \mathrm{km \, s^{-1}}$ trough has also to lie in front of the whole blue side of the Lyα profile, this blue side would be emitted by gas located not only behind the SMGs but also behind the gas causing the absorption at $-550 \, \mathrm{km \, s^{-1}}$, and its negative velocities would be the signature of the inflow of the rear part of the nebula on to the galaxies. It is therefore plausible that the entire Lyα nebula be inflowing towards the galaxies at velocities of several $\times \, 100 \, \mathrm{km \, s^{-1}}$.

This redshift of the CH$^+$ absorption lines, however, could be ascribed to a gas component unrelated to the galaxies. This is unlikely because the CH$^+$ profile in the direction of L2SW-em (Fig. 2) has the characteristic shape of an inverse P-Cygni profile in which the emission and the absorption are linked by the radiative transfer of photons in infalling gas. So, as long as CH$^+$ is concerned, the gas responsible for the emission (i.e. from the UV-irradiated shocks) and that causing absorption (i.e. from the large-scale turbulent reservoir of diffuse molecular gas) are dynamically and radiatively coupled. The gas causing the CH$^+$ absorption and the extended part of the Lyα nebula, at similar velocities and velocity dispersions, are most likely also dynamically linked to the system. We therefore are confident that the gas emitting the redshifted Lyα emission of the nebula is dynamically connected to the system, and is inflowing towards L1 and L2SW.

Last, the mere existence of this extended cool molecular phase moving at the same velocities as the warm phase emitting Lyα indicates that not only they are mixed together i.e. the CGM is multiphase, as said above, but also that they share the same dynamics. However, the Lyα emission probably extends beyond the limits of the KCWI image (Fig. 7) i.e. its radius is >9 arcsec ~ 50 kpc in source plane. It is larger than the radius inferred for the diffuse molecular
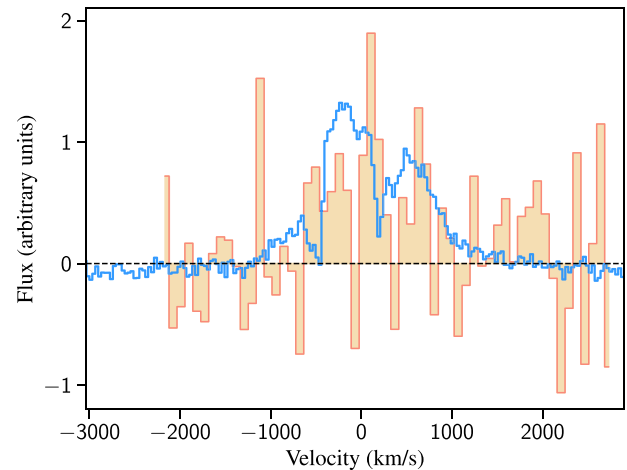

Figure 10. Superposition (in arbitrary units) of the IRAM-30m CH$^+$(1–0) spectrum of SMM J02399−0136 at a spectral resolution of 64 MHz (or $87 \, \mathrm{km \, s^{-1}}$) (beige) and the KCWI Lyα spectrum integrated over the IRAM-30m half-power beamwidth (HPBW = 11.2 arcsec) (blue). The common origin of the velocity scale is computed for $z_{ref} = 2.8041$.

reservoir which suggests that the inflowing gas is molecular only within the inner regions, at distances $\lesssim 20$ kpc. The co-spatiality of these two phases further suggests that some thermal cooling radiation necessarily contributes to the Lyα line emission (Gnat & Ferland 2012).

5.2 The broad CH$^+$ and Lyα emission lines

The Lyα emission has been integrated over the IRAM-30m HPBW=11.2 arcsec to compare its line profile to that of the CH$^+$ emission (Fig. 10). As expected, the line cores differ because
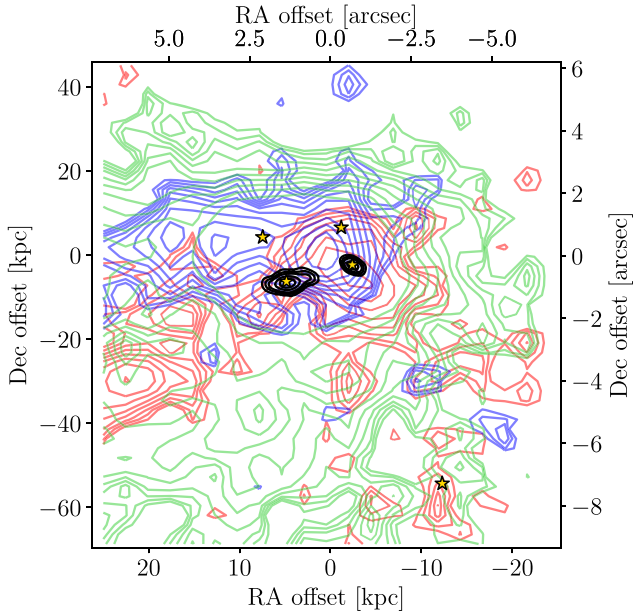
Figure 11. Contours of the Lyα emission integrated over the velocity ranges [0, 500] km s^{-1} (green), [1000, 1500] km s^{-1} (red), and [−1200, −700] km s^{-1} (blue). The contours are at $\log_{10}(\mathrm{SB}_{\mathrm{Ly}\alpha}/[10^{-17}\mathrm{erg\,s^{-1}cm^{-2}arcsec^{-2}}]) = -0.1\,(10-n)$ for the 10 lowest levels, n =1 to 10, and 0.5 and 1 for the two highest, to emphasize the gradients at low brightness. Black contours delineate the continuum sources and the five yellow stars indicate the positions of L1, L2SW, L1N, L2 and L3.

of the vastly different opacities of the two lines (the Einstein coefficients are, respectively, $A_{10} = 5.9 \times 10^{-3}$ s^{-1} for CH$^+$(1–0) and $A_{\mathrm{Ly}\alpha} = 6.265 \times 10^{8}$ s^{-1}), but the similarity of their full extent (FWZI ~ 3000 km s^{-1}) is striking and suggests a shock contribution to the Lyα lines as done in the analysis of another conspicuous ELAN (Cai et al. 2017) and as modelled in self-irradiated shocks (Lehmann et al. 2020a, b). Extremely broad Lyα lines may therefore have a kinematic origin, in parallel to being due to opacity broadening (Faucher-Giguère et al. 2010).

We detail below the rich facets of this similarity, in space and velocity space. The Lyα profiles are complex but their spatial distribution in three different velocity ranges (Fig. 11) is most informative. In the velocity range close to the Lyα line centroid ([0, 500] km s^{-1}, green contours), there is a bright extended plateau with little spatial structure, encompassing the galaxies and co-located with the turbulent reservoir of diffuse gas causing the CH$^+$ absorption (Fig. 7). At the opposite, the contours in the high-velocity (HV) positive ([1000, 1500] km s^{-1}, red) and negative ([−1200, −700] km s^{-1}, blue) ranges are highly structured in space.

Positive velocities are dominating the HV Lyα emission, consistent with primarily outflowing gas according to Lyα radiative transfer (Verhamme et al. 2006; Dijkstra 2017). The geometry of these high positive velocities on each side of L1 and L2SW suggests high opening angles of the outflows.

The overlay of the Lyα HV contours with the CH$^+$ emission structures identified in the ALMA data suggests that these structures are not randomly distributed in space (Fig. 12). They follow the edges (i.e. brightness gradients) of the high-velocity contours, or are found at the tip of elongated Lyα structures. Half of those located within 4.5 arcsec of the phase centre lie in the environment of L1, at projected distances up to ~ 15 kpc in the source plane (see Table 3). Most of the least plausible candidates are clustered to the east of

L2SW, where the positive and negative Lyα high-velocity contours overlap in projection, signposting complex dynamics. Another view of this overlay is given in Appendix E, where the spatial distribution of Lyα high-velocity emissions is compared to CH$^+$ moment-0 maps computed on a spatially smoothed version of the ALMA data. Long and weak structures of CH$^+$ line emission appear that exquisitely follow, in a few cases, the edges of the high-velocity Lyα emissions.

The spatial distribution of the CH$^+$ emission structures with respect to the HV Lyα emissions suggests that they trace molecular shocks located at the thin and highly convoluted interface of the AGN- and starburst-driven outflows (i.e. the high-velocity components of the Lyα line) with the inflowing CGM.

The position–velocity cuts of Fig. 13 offer another projection of the data. There, it is clear that the structures of CH$^+$ emission never share the position and velocity of Lyα peaks, but nevertheless always have a Lyα counterpart, albeit sometimes weak. This finding further supports the shock interpretation of the CH$^+$ emission structures, shifted both in space and velocity from the Lyα peaks. It also highlights the weak contribution of these shocks to the Lyα emission of the nebula. The diversity of the relative positions of the shocks and Lyα emission is due mostly to projection effects. This comparison of the position–velocity distributions of CH$^+$ and Lyα emission suggests that L2SW-ne2, L2SW-se2, and L2SW-se3 are plausible regions of CH$^+$ emission, although located ~ 5 arcsec (or ~ 18 kpc) from the phase centre. In the following, we adopt 18 kpc as the largest distance of the CH$^+$ emission structures from the galaxies.

The observed fact that the broadest Lyα lines are found only in the unresolved brightest part of the nebula, in the vicinity of the BAL QSO L1, might appear in apparent contradiction with the findings of Laursen, Sommer-Larsen & Andersen (2009) who show that, in their simulations of forming galaxies, dust absorption primarily affects the wings of the Lyα lines. This is so because the wings are found to originate in the densest and most opaque parts of the galaxies. It is not the case here and this suggests that the Lyα broad wings in SMM J02399−0136 are not originating in the most opaque regions of this system but in far less compact regions at distances >3.5 kpc from L1, at the interface of powerful galactic winds and the CGM, as suggested in Paper I.

6 DISCUSSION

Thanks to the unique kinematic information carried out jointly by the CH$^+$ and Lyα lines, augmented by the ancillary CO data, we are now able to draw a coherent picture in which a large-scale inflow interacts with powerful AGN- and stellar-driven outflows, and where the mass and energy injection rates from both the galactic winds and gravitational accretion sustain the co-existence over the starburst phase of the massive turbulent CGM and the high star formation rate.

6.1 What CH$^+$, Lyα, and multitransition CO observations tell us

The published CO observations of SMM J02399−01236 are a precious addition to the CH$^+$ – Lyα comparison because they have been carried out in several transitions and at different angular resolutions. For comparison, the velocities and FWHM of the Lyα, CH$^+$, and CO lines are gathered in Table 4 with the respective angular resolution of their observations.

The key kinematic properties of the different components seen in various tracers can be summarized as follows:
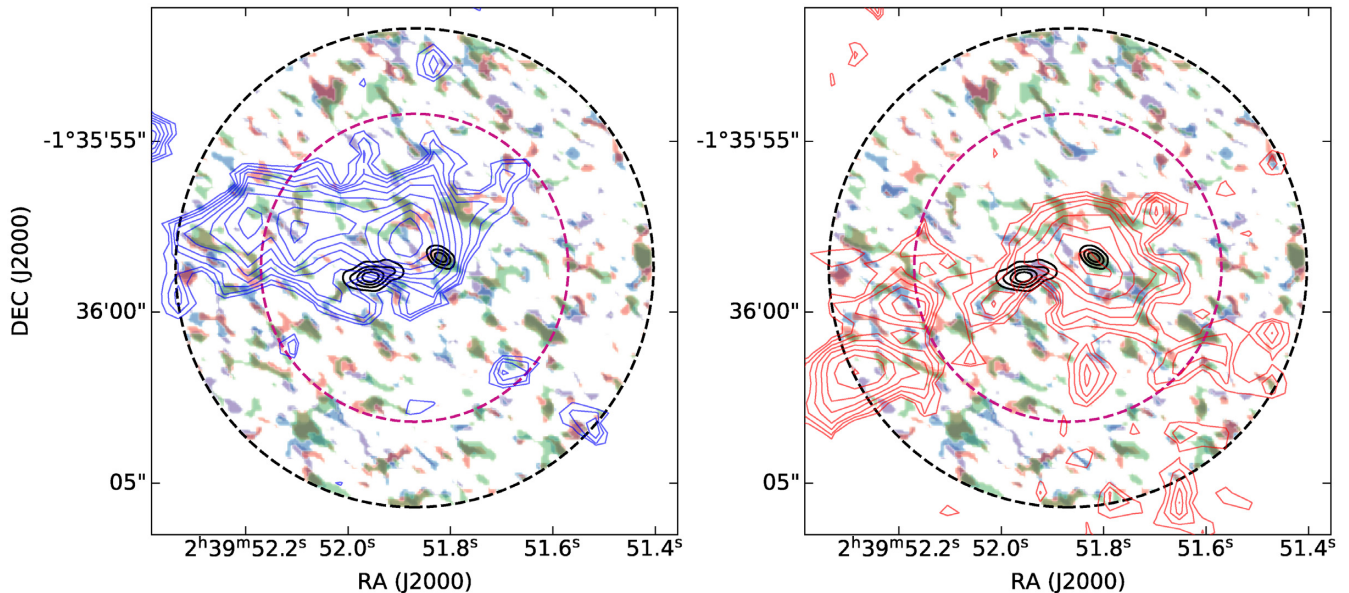
Figure 12. Superposition of the velocity-dependent shapes of the structures of CH$^+$ emission (same as in Fig. 4) tentatively detected at the $1 \times \sigma_{m0}$ level with contours of the Lyα emission integrated over the velocity ranges $[-1200, -700]$ km s^{-1} (blue) (left-hand panel) and $[1000, 1500]$ km s^{-1} (red) (right-hand panel). The origin of the velocity scale is the systemic velocity of the galaxies at $z_{ref} = 2.8041$. The ALMA 1/3 primary beam is shown (black dashed circle) as well as the distance of 4.5 arcsec from the phase centre (dashed magenta circle).

(1) The Lyα line in the direction of L3 and in the bulk of the Lyα nebula, the HV absorption line in the direction of L2SW, the CO(1–0) Green Bank Telescope (GBT) component A and the CO(3–2) ALMA component W1, all have, within the error bars, the same redshifted velocity and about the same FWHM (in boldface in Table 4). These CO and Lyα components extend, up to 6 arcsec and $\gtrsim 10$ arcsec from the galaxies, respectively.

(2) The extremely broad Lyα linewings in the direction of L1 and L2SW, the CH$^+$(1–0) emission in the close vicinity of the galaxies and the CO($J = 7$–6) lines trace highly excited gas. They are centred at the same velocity, ≈ 0 km s^{-1} suggesting that there is some shock contribution to the Lyα and CO(7–6) emissions associated with the close (kpc-scale) environment of the galaxies. We note that the high-J CO line is about twice narrower than the CH$^+$ emission lines. This can be understood by the fact that the abundance of CH$^+$ is enhanced in strong UV fields while CO is photodissociated (Godard et al. 2019).

(3) The average velocity of the CH$^+$ absorptions, $\overline{v}_{abs} = 380 \pm 200$ km s^{-1} is commensurate with those of the CH$^+$ emission lines (Table 3), $\overline{v}_{em} = 170 \pm 540$ km s^{-1} (resp. 412 ± 520 km s^{-1}) for the eight (resp. eleven) most plausible structures.

As the similarities given in (1) are unlikely to be due to a coincidence, we infer that all these gas components, in addition to being projected over a similar large scale area, are sharing the same dynamics i.e. inflow towards the galaxies at $v_{in} \sim 650$ km s^{-1} because the redshifted HV CH$^+$ absorption line in the direction of L2SW is seen in absorption. The inflowing stream is therefore multiphase within the inner ~ 20 kpc, with a hint that the purely atomic (or ionized) hydrogen inflow extends even further than 50 kpc. A shock contribution to the Lyα emission is inferred from (2).

Lastly, point (3), and the fact that the most plausible CH$^+$ emission structures are scattered within a large area around the galaxies (up to distances ~ 18 kpc in the source frame), commensurate with the radius of the diffuse turbulent reservoir, $r_{TR} = 22\,t_{66}$ kpc, further support that the shocks traced by the CH$^+$ emission lines and the

diffuse, highly turbulent, molecular gas are dynamically coupled: the shocks are the signposts of the mechanical fuelling of turbulence by the outflows within the whole CGM. This was already suggested by the inverse-P Cygni profile tentatively detected in the direction of L2SW-em (see Section 5.1).

The velocity coherence of the Lyα extended component at $v_{in} \sim 650$ km s^{-1} over the full observed projected size of the Lyα nebula is striking (Figs 9 and 13). Its linewidth varies however, mostly ~ 500 km s^{-1}, much broader in the Eastern area with a linewidth ~ 1000 km s^{-1} (pv-cut at RA offset $= +5$ arcsec in Fig. 13). This velocity component is dominant in the western part of the galaxy environment seen in CO(3-2) (Genzel et al. 2003; Frayer et al. 2018). Lower velocity components, still inflowing (since redshifted in absorption with respect to z_{ref}), are also present, e.g. the LV CH$^+$ absorption component towards L2SW and the CH$^+$ absorption in the direction of L1. These are also seen in Lyα emission up to 5 arcsec (or ≈ 15 kpc) eastward of L1 and L2SW (Fig. 9). This is why the average inflowing velocity is only $\overline{v}_{in} = 380$ km s^{-1} (Table 2).

These inflow velocities are large compared to what is expected in forming galaxies (Goerdt & Ceverino 2015), but recent improved numerical treatments of shock heating in the halo of massive galaxies show that large amounts of gas cool down and fall at such high velocities (Bennett & Sijacki 2020). We note that the escape velocity $v_{esc} = (2GM_h/R_h)^{1/2}$ at radius 200 kpc of a halo of virial mass $M_h = 5 \times 10^{12}\,M_\odot$ is

$$v_{esc} = 475 \text{ km s}^{-1} \left(\frac{M_h}{5 \times 10^{12}\,M_\odot} \right)^{1/2} \left(\frac{R_h}{200\,\text{kpc}} \right)^{-1/2}. \tag{4}$$

So, the observed inflow velocities could then be the kinematic signature of large scale recycled winds, in which case outflows and inflows would be intimately mixed (Herrera-Camus et al. 2020). Galactic winds do generate turbulence and a fraction of the expelled matter is susceptible, if enabled to cool down, to fall back on to the galaxies at large velocities (e.g. Gabor & Bournaud 2014).
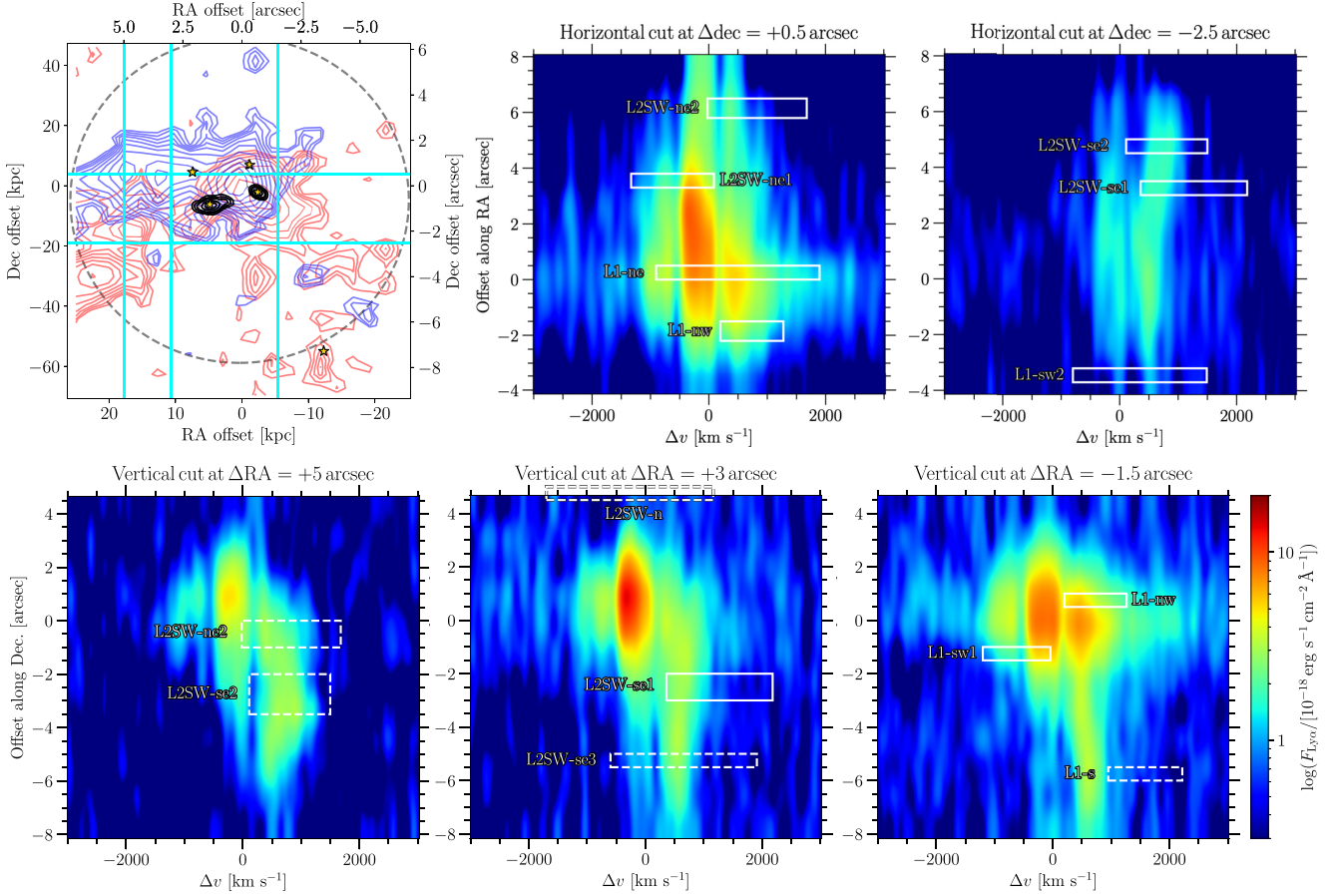
Figure 13. Position–velocity cuts of the Lyα emission along five directions (shown in the upper left-hand panel) crossing the scattered structures of CH⁺ emission. The position and extents in space (full size at the σ_{m0} level) and velocity (FWHM of the CH⁺ line) of each of them is displayed as a white box, next to each name. Dashed boxes mark the five least plausible structures listed in Table 3. Some of them are sampled in two different cuts. The common origin of the velocity scale is computed for $z = 2.8041$.

Table 4. Comparison of the kinematic properties of the low and high excitation phases seen by the Lyα, CH⁺, and CO lines set at the systemic redshift $z_{ref} = 2.8041$ (only the error bars relevant to the discussion are reported).

Line	Telescope	Beam (arcsec)	z_{obs}	Source Component	v_{abs} (km s⁻¹)	Δv_{abs} (km s⁻¹)	v_{em} (km s⁻¹)	Δv_{em}	Reference
Lyα	KCWI	1.5 (seeing)	2.8048	L1	–	–	≈ 0 [a]	≈ 1500	b
				L2SW	–	–	≈ 0	≈ 1500	
				L3	–	–	670 ± 6	353 ± 15	b
CH⁺(1–0)	ALMA	0.36×0.59	2.803	L2SW LV	280	210	–	–	c
				L2SW HV	660 ± 70	290 ± 160	–	–	
				L2SW LV+HV	430	580	–	–	
				L2SW-w	600	750	-10	1280	
				L1-sw	80	290	10	1350	
				Scattered structures	–	–	-600 to 1600	1000 to 3000	
				Average	380 ± 200	490	170 ± 540	1330 ± 270	
	IRAM-30m	11.2			–	–	105 ± 170	1300 ± 500	
CO(1-0)	GBT	25	2.808	A	–	–	637 ± 15	260 ± 35	d
				B	–	–	57 ± 35	660 ± 100	
CO(7-6)	ALMA	0.6×0.5		L1, L2SW	–	–	0	≈ 650	d,e
CO(3-2)	OVRO	7.4×4.8	2.808		–	–	307 ± 158	710 ± 80	f
	IRAM-PdBI	5.2×2.4	2.808		–	–	≈ 100	≈ 900	g
	IRAM-30m	22	2.803		–	–	160 ± 60	800 ± 100	b
	ALMA	0.72×0.61	2.808	W1	–	–	~ 650	~ 260	d

[a]The line is non-Gaussian and its extremely broad red wing makes its first moment positive (see the text). [b]Li et al. (2019). [c]This work. [d]Frayer et al. (2018). [e]From a sentence in Frayer et al. (2018) stating that the CO(7–6) lines detected by ALMA have a similar FWHM as the GBT component B in CO(1–0). [f]Frayer et al. (1998). [g]Genzel et al. (2003).

The turbulent velocity of the inflowing gas $\overline{v}_{\rm turb,TR} = 340\,{\rm km\,s^{-1}}$ is also very large and traces highly supersonic turbulence, even in gas at $T \sim 10^4$ K. The processes susceptible to sustain this high level of large-scale turbulence are AGN- and stellar-driven winds from L1 and L2SW (Faucher-Giguère & Quataert 2012; Costa et al. 2020; Nims, Quataert & Faucher-Giguère 2015) but also gravitational energy either from the merger (Oh, Kim & Lee 2015; Blecha et al. 2018; Biernacki & Teyssier 2018; Bustamante et al. 2018) – the SMM J02399 − 0136 galaxy group being an archetypal example of a merger – or recycled outflows or infalling cold streams (Dekel et al. 2009; Narayanan et al. 2015). This alternative may just be two facets of the same process since galaxies are already forming in accreting cold streams (e.g. Narayanan et al. 2015). Not unexpectedly, Bennett & Sijacki (2020) show that the improvement in the resolution of accretion shocks causes CGM turbulence to increase dramatically, up to values comparable to those observed here.

The inflowing gas could be pristine gas infalling in the dark matter potential well of the galaxies, at large radii where only the Lyα line is detected i.e. $\gtrsim 40$ kpc from the galaxies. The inner part, rich in CO and detected in CH+ is metal-enriched and could be part of recycled outflows. We discuss these possibilities in the next sections, relying on the CH+ and Lyα line observations.

6.2 Where inflow meets outflows

The faster Lyα outflow at $v_{\rm out,1} > 3000\,{\rm km\,s^{-1}}$, originating in L1, and to a lesser extent L2SW, is clearly visible in the position-velocity cut of Fig. 9. It is unresolved and is therefore confined within the inner 0.75 arcsec (or ≈ 3 kpc) environment of the galaxies. We show below that the CH+ and Lyα emission lines make it possible to outline the fate of less powerful outflows, at $v_{\rm out,2} < v_{\rm out,1}$ at distances at least as large as ~ 20 kpc from the galaxies.

The longest structures of broad and weak CH+ emission obtained in the smooth moment-0 maps (Fig. E1) are close to the maximum recoverable size of ~ 5 arcsec, i.e. ~ 15 to ~ 40 kpc in the source plane. Such large lengths and large velocity dispersions are reminiscent of the cold gas kinematic properties observed in the 50-kpc long high-velocity shock (HVS) of the Stephan's Quintet (SQ) where the velocity dispersion of the molecular gas in the post-shock layer of the HVS is that of myriad low-velocity molecular shocks (LVMS). This large dispersion spans the full velocity difference between the colliders, i.e. the intruder galaxy and the H I tidal stream (Guillard et al. 2012, 2021).

Here, the CGM into which the outflows penetrate is inflowing at the projected velocity $\overline{v}_{\rm in} = +380\,{\rm km\,s^{-1}}$. The HVS post-shock extent in velocity, provided by the CH+ linewidths, ranges from 1000 to 3000 km s^{-1} (Table 4). From its average value, $\overline{\Delta v}_{\rm em} = 1330\,{\rm km\,s^{-1}}$, and $\overline{\Delta v}_{\rm em} = |v_{\rm in} - v_{\rm out,2}|$, we infer $v_{\rm out,2} \sim 1000\,{\rm km\,s^{-1}}$ with a large scatter due to projection effects. It is remarkable that this estimate of a characteristic outflow velocity, based on CH+ line emission, falls in the ranges of the blue and red high velocity Lyα emissions (Fig. 11). Their complex geometry prevents more accurate estimates. The CH+ linewidths also yield the velocity of the large scale HVS that is close to the relative velocity of the colliders, $v_{\rm HVS} \sim 1300\,{\rm km\,s^{-1}}$.

Interestingly, the 122 μm [N II] line was detected with the 10.4m telescope of the Caltech Submillimeter Observatory of same HPBW at that frequency as the IRAM-30m telescope (Ferkinhoff et al. 2011) while almost resolved out in subsequent ALMA observations (Ferkinhoff et al. 2015). The similarity of the [N II] and CH+ velocities and velocity coverages over the same area supports an origin of the [N II] line in which nitrogen would be collisionally excited in the HVS shocks rather than photoionized by hard-UV photons.

Now, the CH+ emission brings a new perspective on these kpc-scale HVS. Shocks at high Mach number, in which the magnetic field does not store a large fraction of the pre-shock kinetic energy, heat the post-shock medium to a temperature

$$T = \frac{3\mu_{\rm p} m_{\rm H}}{16 k_{\rm B}} v_{\rm sh}^2 \sim 5 \times 10^7 {\rm K} \left(\frac{v_{\rm sh}}{1300\,{\rm km\,s^{-1}}} \right)^2 \qquad (5)$$

in a monoatomic gas with a mean molecular weight per particle $\mu_{\rm p}$ = 1.3 (Spitzer 1968). This is equivalent to say that half the pre-shock kinetic energy density is transformed into thermal energy density in the post-shock gas.

It is not the case here since, as in the SQ shock, the molecules would not survive, nor reform fast enough, at such high temperatures. The width of the CH+ lines is not thermal but has to trace fast turbulent motions of dense gas. Indeed, the mean turbulent velocity of the LVMS within the post-shock layer of the HVS, $0.7\,\overline{\Delta v}_{\rm em} \sim 900\,{\rm km\,s^{-1}}$, is commensurate with the sound velocity $c_{\rm S} \sim 750\,{\rm km\,s^{-1}}$ of the HVS post-shock layer heated at $\sim 5 \times 10^7$ K indicating that these turbulent motions of the LVMS within this HVS post-shock layer are about trans-sonic.

The physics of such a turbulent cascade through gas phases of temperatures ranging from $\gtrsim 10^7$ to 100 K is still unknown although beautiful observations have started to stress the importance of turbulence, even in the hot intracluster gas (Zhuravleva et al. 2014, 2019; Li et al. 2020). The existence of dense gas within AGN-driven shocks is consistent with theoretical predictions (Richings & Faucher-Giguère 2018a, b; Costa et al. 2020). What is new here is that a fraction of the HVS kinetic energy is not thermalized at $T > 10^7$ K, and therefore radiated in X-rays or highly excited lines of ions, but stored in the extremely fast trans-sonic motions of dense molecular gas i.e. the post-shock layers of the LVMS, emitting the CH+ lines.

The cascade of kinetic energy has to proceed up to the stage where the turbulent motions drive shocks at $v_{\rm sh} \sim 20\,{\rm km\,s^{-1}}$, enabled to efficiently form CH+. It involves a broad distribution of shock velocities, from $v_{\rm sh} \sim 1300$ to 20 km s^{-1}, propagating in a variety of pre-shock densities and gas phases.

In summary, although they are only individual tentative detections, the spatially scattered and broad CH+ emission lines, when analysed in conjunction with the Lyα high-velocity field and morphology, can be understood as tracing kpc-scale HVS at $\overline{v}_{\rm HVS} \sim 1300\ {\rm km\,s^{-1}}$ formed at the interface of AGN- and stellar-driven outflows at $\overline{v}_{\rm out,2} \sim 1000\,{\rm km\,s^{-1}}$ and inflowing CGM at $\overline{v}_{\rm in} \sim 400\,{\rm km\,s^{-1}}$, up to distances as large as ~ 20 kpc from the galaxies (in projection). Interestingly, the standard deviation of their projected velocities, $\sigma_{v_{\rm em}} = 540\,{\rm km\,s^{-1}}$ (Table 3) corresponds to a mean turbulent velocity of their ensemble $1.6\sigma_{v_{\rm em}} \sim 900\,{\rm km\,s^{-1}}$, close to $\overline{v}_{\rm out,2}$.

6.3 Following the energy trails: radiative, turbulent and gravitational luminosities

The above results confirm the multiphase nature of the cold CGM, including cool diffuse and cold dense molecular phases, in addition to the hot and warm phases, over large distances from the galaxies. They also disclose not only the high level of turbulence in the massive CGM but also how and where the stellar- and AGN-driven outflows inject kinetic energy into the CGM (i.e. the myriad shocks seen in CH+ emission).

The two questions raised by these results are therefore: (i) are these outflows able to sustain the turbulence observed in such a massive

cold CGM over the starburst phase duration? and (ii) are they able to compensate the mass drain of the cold CGM due to the high star formation rate?

The cold phases of the CGM comprise the cool diffuse molecular gas of mass M_{TR} inferred from CH^+ absorption and denser molecular gas of mass M_{CO} seen as extended CO(1-0) emission with the EVLA (Ivison et al. 2010a) and the GBT (Frayer et al. 2018). Its turbulent luminosity is $L_{turb,cCGM} = \frac{1}{2} M_{TR} \bar{v}_{turb,TR}^2 / t_{dyn} + \frac{1}{2} M_{CO} \bar{v}_{turb,CO}^2 / t_{dyn}$, where the dynamical time t_{dyn} should be similar for the two components.

For the diffuse gas, $M_{TR} = 3.7 \times 10^{10} t_{66}^2$ $M_\odot$ and $\bar{v}_{turb,TR} = 340 \, km \, s^{-1}$ (Table 2) so that $L_{turb,TR} = 2.2 \times 10^{43} t_{66}$ erg s^{-1} with $t_{66} = t_{dyn}/66$ Myr. The mass of the denser component extending over ~ 25 kpc, $M_{CO} = 1.7 \times 10^{11}$ $M_\odot$, is the mass of the low-excitation component that contributes 75 per cent of the total mass seen in CO(1-0). We adopt the linewidth measured by Frayer et al. (2018) for the low-excitation CO emission, $\Delta v_{CO} = 260 \, km \, s^{-1}$, so that $\bar{v}_{turb,CO} = 182 \, km \, s^{-1}$, and $L_{turb,CO} \sim 2.8 \times 10^{43} t_{66}^{-1}$ erg s^{-1}. Note that $t_{dyn} = 68$ Myr for that low-excitation CO component. The turbulent luminosity of the cool and cold CGM (hereafter cold CGM) is therefore $L_{turb,cCGM} \sim 5 \times 10^{43}$ erg s^{-1} for $t_{66} = 1$.

We now estimate the mechanical luminosity of the stellar- and AGN-driven outflows from the luminosity of the $CH^+(J = 1-0)$ emission lines, relying on models of UV-irradiated molecular shocks (Godard et al. 2019). The $CH^+(J = 1-0)$ integrated line flux of all the shocks detected by IRAM-30m, $S_{CH^+} \Delta v = 4.7$ Jy km s^{-1} (see Section 3.2), corresponds to a line luminosity, $\mu L_{CH^+(1-0)} = 2.3 \times 10^{42}$ erg s^{-1}, at the luminosity distance of SMM J02399−0136, $D_L = 24.0$ Gpc (Solomon et al. 1997). As in the UV-irradiated shock models of Godard et al. (2019), the $J = 1-0$ transition is found to contribute about 20 per cent of the energy radiated by all the CH^+ rotational transitions, the total CH^+ line luminosity, $L_{CH^+} \sim 6.5 \times 10^{42}$ erg s^{-1} (after correction for lensing), is as large as ~ 5 per cent of the Lyα luminosity, $L_{Ly\alpha} = 1.4 \times 10^{44}$ erg s^{-1} (Li et al. 2019). In these shock models, the total flux radiated in the CH^+ lines follows the kinetic energy flux entering the shocks, with different ratios $f_{CH^+,kin} = L_{CH^+}/L_{kin,sh}$ depending on the pre-shock densities, the shock velocities and UV irradiations. For shock velocities $v_{sh} \geq 10 \, km \, s^{-1}$ and an UV irradiation $G_0 = 10^4$, this ratio increases sharply between 5×10^{-4} and 10^{-2} for pre-shock densities between 5×10^4 and 10^5 cm^{-3} that are the most appropriate conditions to explain the CH^+ line intensities (Appendix D). Estimates of this ratio for molecular shocks at higher velocities will be published in a forthcoming paper (Lehmann et al. submitted) but these higher velocity shocks are J-shocks, much less efficient to form CH^+.

The UV-irradiation of the CGM at distances of several $\times 10$ kpc from the galaxies is difficult to estimate. However, values as high as $G_0 = 10^4$ or larger, even at distances $d \sim 20$ kpc from L1, are expected in the case of SMM J02399−0136, given the illumination of the dark-cloud L3 located at ~ 60 kpc from L1 (Li et al. 2019). The bolometric luminosity of SMM J02399−0136 is $L_{bol} = 1.2 \times 10^{13}$ L$_\odot$ (Ivison et al. 2010a). As the AGN contributes 42 per cent of the total FIR luminosity and assuming that the difference between L_{bol} and L_{FIR} is entirely due to the AGN, we infer $L_{bol,AGN} = 2.8 \times 10^{46}$ erg s^{-1}. The UV-luminosity below 912 Å is $\sim 0.25 \times L_{bol}$ (Li et al. 2019), so that the flux of UV photons expressed in Habing units[6] at a distance d_{20} of 20 kpc from L1 depends only on the solid angle Ω_{free} of the quasi dust-free lanes opened up by the AGN-driven winds and

responsible from the large anisotropy of UV photons around QSOs:

$$G_0 = 1.5 \times 10^5 \left(\frac{\Omega_{free}}{0.1} \right)^{-1} d_{20}^{-2}. \tag{6}$$

We note that Li et al. (2019) find $\Omega_{free} \sim 0.07$ for the UV-irradiation in the direction of the L3 dark-cloud at 60 kpc from L1. The UV-luminosity of the AGN alone is therefore sufficient to provide $G_0 \geq 10^4$ over several regions located at the tip of dust-free lanes around L1, to which the contribution of the L2SW starburst should be added. The anisotropy of the UV field at large scale around these galaxies is supported by the scattered structure of the visible spots in Fig. 1.

In the following, we therefore adopt $G_0 = 10^4$ as a lower limit of the shock UV-irradiation in the CGM at distances ~ 20 kpc from the galaxies and the upper limit $f_{CH^+,kin} = 10^{-2}$ that provides a lower limit to the kinetic luminosity of the ensemble of LVMS, $L_{kin,sh} = L_{CH^+}/f_{CH^+,kin} > 6.5 \times 10^{44}$ erg s^{-1}. This is an immense kinetic luminosity that signposts the terminal dissipative step of the energy cascade triggered, within their post-shock layers, by the HVS. Assuming mass and energy flux conservation between HVS and the myriad LVMS and neglecting the radiative losses in the warm gas that are much smaller than the total Lyα luminosity, a massive molecular outflow rate is inferred from $L_{kin,sh} = \frac{1}{2} \dot{M}_{out} v_{out,2}^2$:

$$\dot{M}_{out} > 2 \times 10^3 \, M_\odot \, yr^{-1} \left(\frac{v_{out,2}}{10^3 \, km \, s^{-1}} \right)^{-2}, \tag{7}$$

leading to a mass loading factor $\dot{M}_{out}/SFR > 2.4$ in the range of those observed for high-z starburst galaxies (Veilleux et al. 2020). The spatial pattern of the high-velocity Lyα emissions (Fig. 11) supports a joint AGN and starburst driving of the galactic outflows. Indeed, Biernacki & Teyssier (2018) show that only the non-linear coupling of AGN and supernovae feedbacks is able to produce massive and extended outflows.

As the AGN contribution to the kinetic luminosity is necessarily smaller than the above value, we find that $L_{kin}^{AGN} < 0.02 \, L_{bol,AGN}$, an upper limit broadly consistent with the values inferred from numerical simulations of AGN-driven large-scale outflows, $L_{kin} = 0.004 \, L_{AGN}$ (Costa et al. 2020).

Even taking into account the ~ 10 per cent of the shock energy dissipated in the LVMS and radiated in the H_2 lines (Godard et al. 2019), the kinetic luminosity estimated above, $L_{kin,sh} > 6.5 \times 10^{44}$ erg s^{-1}, is more than $10 \times$ larger than that needed to sustain the cold CGM turbulence within a radius ~ 20 kpc and over the starburst lifetime. The mass outflow rate sufficient to feed the cold CGM turbulent luminosity, $L_{turb,cCGM} = 5 \times 10^{43}$ erg s^{-1}, is therefore much smaller than $\dot{M}_{out}$:

$$\dot{M}_{out,cCGM} \sim 150 \, M_\odot \, yr^{-1} \left(\frac{v_{out,2}}{10^3 \, km \, s^{-1}} \right)^{-2}. \tag{8}$$

A net mass inflow rate into the cold CGM, $\dot{M}_{in,cCGM} = SFR - \dot{M}_{out,cCGM} \sim 720 \, M_\odot \, yr^{-1}$, is required to reach a steady state, where the cold CGM mass drain due to star formation is compensated jointly by the outflows and the gas inflow. This net mass inflow to the CGM of the galaxy group could be due to the gas tidal streams of the galaxy merger. However, in numerical simulations, tidal streams due to mergers are not found as massive and extended as what is observed here, and are most often seen as outflows, not inflows (Narayanan et al. 2006). The net mass inflow could also be due to gas expelled further away than ~ 20 kpc from the galaxies by the powerful galactic winds, falling back on to the inner CGM if it succeeds at cooling efficiently. Last, it could be due to cold stream accretion on to the host halo of this galaxy group.

---

[6]Habing flux integrated between 912 and 2066 Å, $F_\lambda \Delta\lambda = 1.3 \times 10^{-4}$ erg s^{-1} cm^{-2} sr^{-1}.

We therefore speculate that the missing mass contribution, $\dot{M}_{\rm in,CGM} \sim 720\,{\rm M_\odot\,yr^{-1}}$, whatever its origin, is due to net gas accretion into the inner gravitational potential well of the galaxy group and that the gravitational cooling rate from this infalling material is an additional energy source of the cold CGM turbulence. The gravitational luminosity estimated at a representative distance d from the galaxies

$$L_{\rm grav} = \frac{G\dot{M}_{\rm in,CGM} M_{\rm stars}}{d} \tag{9}$$

for $M_{\rm stars} = 7 \times 10^{11}\,{\rm M_\odot}$ (Aguirre et al. 2013) appears to be also comparable to all the other luminosities:

$$L_{\rm grav} = 3.7 \times 10^{43}\,{\rm erg\,s^{-1}}\ \frac{\dot{M}_{\rm in,CGM}}{720\,{\rm M_\odot\,yr^{-1}}}\frac{M_{\rm stars}}{7\times10^{11}\,{\rm M_\odot}}\left(\frac{d}{40\,{\rm kpc}}\right)^{-1} \tag{10}$$

where the infalling time from distance ~ 40 kpc at $v_{\rm in} = 400\,{\rm km\,s^{-1}}$ is still commensurate with the estimated duration of the starburst phase. The gravitational energy is therefore another contribution to the feeding of turbulence of the massive CGM, and as such, it is also eventually lost by radiation in the cool phase, locally heated by turbulent dissipation and producing CH$^+$ in the diffuse CGM.

These results reveal the critical role of turbulence in reprocessing the different sources of energy, were they AGN- and starburst-driven outflows or large-scale gravitational energy of infalling streams, down to the kinetic and thermal energy of the cool phase, in which this energy is eventually radiated and lost.

All the above rates are order-of-magnitude estimates in agreement with the model of Bouché et al. (2010). They show that, although a merger is accelerating the process of star formation in this system, the star formation and black-hole growth are most likely fuelled, ultimately, by large-scale accretion. It is not possible, at this stage to distinguish the origin of the infalling gas, namely cold stream accretion or recycled outflows. Any infalling gas of low metallicity may just be indistinguishable in the inner tens of kpc of the CGM because it is mixed with powerful outflows and metal-enriched by small-scale turbulent mixing, as shown in numerical simulations (e.g. Shen et al. 2013). As a final note, it is fascinating to observers that the theoretical predictions for the total mass inflow rate on to the host halo (Dekel et al. 2009), and the numerical results for both the smooth and merger-based baryon accretion efficiencies at redshift $z = 2.8$ (Wright et al. 2020), $\dot{M}_{\rm grav} = 740\,{\rm M_\odot\,yr^{-1}}$ be so close to our estimated infall rate $\dot{M}_{\rm in,cCGM}$ for a halo mass $M_{\rm h} = 4.5 \times 10^{12}\,{\rm M_\odot}$, and a cosmological baryon fraction $f_b = 0.165$. If not due to chance, this would suggest that the contribution of recycled outflows to the gas infall in this galaxy group is low.

7 SUMMARY AND OPEN QUESTIONS

Unexpectedly, the CH$^+$ and Lyα lines observed, at high angular and spectral resolution, towards the galaxy group SMM J02399−0136 provide coherent and complementary information on the dynamics of the multiphase CGM. The main results are summarized as follows:

(i) The co-existence of the two cool and warm thermal phases up to distances ~ 20 kpc in the CGM of the galaxies validates, in this case, the critical assumptions made to interpret the CH$^+$ absorption lines detected against the continuum emission of several starburst galaxies (Paper I). It supports the turbulent framework itself and the link between the CH$^+$ abundance in diffuse gas and the turbulent dissipation rate.

(ii) Inflow of the massive, multiphase, highly turbulent CGM towards the galaxies at an average velocity $\overline{v}_{\rm in} \sim 380\,{\rm km\,s^{-1}}$ is

ascertained, from both the redshifted CH$^+$ absorption with respect to the velocity of the galaxies and the detailed comparison of the Lyα, CH$^+$, and CO line profiles.

(iii) Multiple kpc-scale shocks are tentatively detected as broad CH$^+$ emission lines ($\Delta v_{\rm em} = 1300\,{\rm km\,s^{-1}}$ on average) at the interface of the inflowing CGM and the high-velocity Lyα emission of galactic winds from the AGN and the starburst galaxy. They are scattered in the CGM, up to ~ 20 kpc from the galaxies. They trigger turbulent cascades in the post-shock gas, generating a hierarchy of shocks, from the high-velocity shocks (HVSs) at $\gtrsim 1000\,{\rm km\,s^{-1}}$ down to the low-velocity molecular shocks at $\gtrsim 20\,{\rm km\,s^{-1}}$, where CH$^+$ can form efficiently. The HVS kinetic energy density is not fully thermalized in the post-shock layer.

(iv) While the immense kinetic luminosity of the shock ensemble signposts powerful AGN- and starburst-driven outflows likely enabled to eject considerable amounts of gas out of the galaxies' potential well, only ~ 10 per cent of this kinetic luminosity is required to sustain turbulence in the cold CGM. However, a net mass accretion, at a rate $\dot{M}_{\rm in,cCGM} \sim 720\,{\rm M_\odot\,yr^{-1}}$ is required to balance the mass drain of the cold CGM due to star formation. The loss of gravitational energy of this infalling gas is an additional energy source for the CGM turbulence.

These results, obtained in the galaxy group of SMM J02399−0136, illustrate the invaluable complementarity of the Lyα lines and molecular line tracers, as different as high-*J* CO and CH$^+$ lines, in unravelling not only the complex physics of the turbulent, multiphase CGM, but also the disheartening intricacy of the Lyα radiative transfer. They suggest that there is thermal cooling and shock contributions to the Lyα emission.

Because of a conjunction of three unrelated properties, i.e. its highly endothermic formation, its UV-driven abundance enhancement, and its high dipole moment, CH$^+$ is a very unique molecular species that provides a wealth of clues inaccessible to other tracers. The CH$^+$ lines not only trace the presence of diffuse molecular gas, of density marginally able to excite the low-*J* CO lines, but also highlight the bursts of dissipation of mechanical energy, either in emission in UV-irradiated shocks where CO is photodissociated or in absorption on the sites of intermittent dissipation of turbulence in the cool diffuse gas.

These results reveal the critical role of turbulence in channelling energy and momentum across gas phases and scales, drastically modifying the time-scales over which the energy is lost by radiation. The amount of energy stored in fast turbulent motions of cool gas and eventually radiated in low-excitation lines has probably been broadly underestimated.

Lastly, some fine tuning in terms of mass and energy seems to be at work in this galaxy group between the AGN and stellar feedback, the gravitational infall, and the star formation rate. While the starburst phase is triggered by the galaxy merger, the steady state suggested by the existence of the massive turbulent reservoir of cool gas, i.e. the cold CGM, requires large-scale accretion.

It remains an open issue how the gravitational potential energy is shared between the turbulent and thermal energy of the warm and cool gas in the CGM. This can be addressed with future observations of the cooling radiation of the diffuse molecular gas, i.e. the [C II] line – unfortunately not accessible to ground-based telescopes at the redshift of this source – and the pure rotational lines of H$_2$). We face a similar issue for the prodigious shock kinetic energy, at the interface

of galactic outflows and the CGM, with the additional complexity borne by the the multiphase nature of the post-shock gas.

DATA AVAILABILITY

This paper makes use of the data under project numbers ADS/JAO.ALMA#2016.1.00282.S (ALMA), U128 (Keck/KCWI), and 086-19 (IRAM-30m). They are all publicly available in the corresponding archives.

REFERENCES

Aguirre P., Baker A. J., Menanteau F., Lutz D., Tacconi L. J., 2013, ApJ, 768, 164
Agúndez M., Goicoechea J. R., Cernicharo J., Faure A., Roueff E., 2010, ApJ, 713, 662
Amano T., 2010, ApJ, 716, L1
Appleton P. N. et al., 2013, ApJ, 777, 66
Appleton P. N. et al., 2017, ApJ, 836, 76
Arrigoni Battaia F., Prochaska J. X., Hennawi J. F., Obreja A., Buck T., Cantalupo S., Dutton A. A., Macciò A. V., 2018, MNRAS, 473, 3907
Bennett J. S., Sijacki D., 2020, MNRAS, 499, 597
Berta S. et al., 2021, A&A, 646, A122
Bielby R. M. et al., 2020, MNRAS, 493, 5336
Biernacki P., Teyssier R., 2018, MNRAS, 475, 5688
Blecha L., Snyder G. F., Satyapal S., Ellison S. L., 2018, MNRAS, 478, 3056
Bouché N. et al., 2010, ApJ, 718, 1001
Bouché N., Murphy M. T., Kacprzak G. G., Péroux C., Contini T., Martin C. L., Dessauges-Zavadsky M., 2013, Science, 341, 50
Bussmann R. S. et al., 2013, ApJ, 779, 25
Bustamante S., Sparre M., Springel V., Grand R. J. J., 2018, MNRAS, 479, 3381
Cai Z. et al., 2017, ApJ, 837, 71
Carilli C. L., Walter F., 2013, ARA&A, 51, 105
Carter M. et al., 2012, A&A, 538, A89
Costa T., Pakmor R., Springel V., 2020, MNRAS, 497, 5229
Davé R., Crain R. A., Stevens A. R. H., Narayanan D., Saintonge A., Catinella B., Cortese L., 2020, MNRAS, 497, 146
Dekel A. et al., 2009, Nature, 457, 451
Diego J. M., Broadhurst T., Wong J., Silk J., Lim J., Zheng W., Lam D., Ford H., 2016, MNRAS, 459, 3447
Dijkstra M., 2017, preprint (arXiv:1704.03416)
Douglas A. E., Herzberg G., 1941, ApJ, 94, 381
Draine B. T., 1986, ApJ, 310, 408
Eales S. et al., 2010, PASP, 122, 499
Faisst A. L. et al., 2020, ApJS, 247, 61
Falgarone E., Hily-Blant P., Levrier F., 2004, Ap&SS, 292, 89
Falgarone E. et al., 2017, Nature, 548, 430 (Paper I)

Faucher-Giguère C.-A., Quataert E., 2012, MNRAS, 425, 605
Faucher-Giguère C.-A., Kereš D., Dijkstra M., Hernquist L., Zaldarriaga M., 2010, ApJ, 725, 633
Federman S. R., Rawlings J. M. C., Taylor S. D., Williams D. A., 1996, MNRAS, 279, L41
Ferkinhoff C. et al., 2011, ApJ, 740, L29
Ferkinhoff C., Brisbin D., Nikola T., Stacey G. J., Sheth K., Hailey-Dunsheath S., Falgarone E., 2015, ApJ, 806, 260
Flower D. R., Roueff E., Zeippen C. J., 1998, J. Phys. B At. Mol. Phys., 31, 1105
Frayer D. T., Ivison R. J., Scoville N. Z., Yun M., Evans A. S., Smail I., Blain A. W., Kneib J.-P., 1998, ApJ, 506, L7
Frayer D. T. et al., 1999, ApJ, 514, L13
Frayer D. T., Maddalena R. J., Ivison R. J., Smail I., Blain A. W., Vanden Bout P., 2018, ApJ, 860, 87
Fu H., Xue R., Prochaska J. X., Stockton A., Ponnada S., Lau M. W., Cooray A., Narayanan D., 2021, ApJ, 908, 188
Fujimoto S. et al., 2019, ApJ, 887, 107
Gabor J. M., Bournaud F., 2014, MNRAS, 441, 1615
Gaspari M., Ruszkowski M., Oh S. P., 2013, MNRAS, 432, 3401
Gaspari M., Temi P., Brighenti F., 2017, MNRAS, 466, 677
Gavazzi R. et al., 2011, ApJ, 738, 125
Genzel R., Baker A. J., Tacconi L. J., Lutz D., Cox P., Guilloteau S., Omont A., 2003, ApJ, 584, 633
Gerin M., Neufeld D. A., Goicoechea J. R., 2016, ARA&A, 54, 181
Gnat O., Ferland G. J., 2012, ApJS, 199, 20
Godard B., Cernicharo J., 2013, A&A, 550, A8
Godard B., Falgarone E., Pineau des Forêts G., 2009, A&A, 495, 847
Godard B., Falgarone E., Pineau des Forêts G., 2014, A&A, 570, A27
Godard B., Pineau des Forêts G., Lesaffre P., Lehmann A., Gusdorf A., Falgarone E., 2019, A&A, 622, A100
Goerdt T., Ceverino D., 2015, MNRAS, 450, 3359
Gredel R., van Dishoeck E. F., Black J. H., 1993, A&A, 269, 477
Greve T. R. et al., 2005, MNRAS, 359, 1165
Gronke M., Oh S. P., 2020, MNRAS, 494, L27
Guillard P. et al., 2012, ApJ, 747, 95
Guillard P. et al., 2021, preprint (arXiv:2102.06843)
Hafen Z. et al., 2019, MNRAS, 488, 1248
Herrera-Camus R. et al., 2020, A&A, 633, L4
Hodge J. A., da Cunha E., 2020, R. Soc. Open Sci., 7, 200556
Hopkins P. F. et al., 2018, MNRAS, 480, 800
Ikarashi S. et al., 2017, ApJ, 849, L36
Indriolo N., Bergin E. A., Falgarone E., Godard B., Zwaan M. A., Neufeld D. A., Wolfire M. G., 2018, ApJ, 865, 127
Ivison R. J., Smail I., Le Borgne J.-F., Blain A. W., Kneib J.-P., Bezecourt J., Kerr T. H., Davies J. K., 1998, MNRAS, 298, 583
Ivison R. J., Smail I., Papadopoulos P. P., Wold I., Richard J., Swinbank A. M., Kneib J. P., Owen F. N., 2010a, MNRAS, 404, 198
Ivison R. J. et al., 2010b, A&A, 518, L35
Ivison R. J., Papadopoulos P. P., Smail I., Greve T. R., Thomson A. P., Xilouris E. M., Chapman S. C., 2011, MNRAS, 412, 1913
Johnson T. L., Sharon K., Bayliss M. B., Gladders M. D., Coe D., Ebeling H., 2014, ApJ, 797, 48
Kennicutt Robert C. J., 1998, ApJ, 498, 541
Laursen P., Sommer-Larsen J., Andersen A. C., 2009, ApJ, 704, 1640
Lehmann A., Godard B., Pineau des Forêts G., Falgarone E., 2019, Proceedings of the International Astronomical Union, 15, 73
Lehmann A., Godard B., Pineau des Forêts G., Falgarone E., 2020b, A&A, 643, A101
Lesaffre P., Pineau des Forêts G., Godard B., Guillard P., Boulanger F., Falgarone E., 2013, A&A, 550, A106
Li Q. et al., 2019, ApJ, 875, 130
Li Y. et al., 2020, ApJ, 889, L1
Lochhaas C., Bryan G. L., Li Y., Li M., Fielding D., 2020, MNRAS, 493, 1461
Lotz J. M. et al., 2017, ApJ, 837, 97
Madau P., Dickinson M., 2014, ARA&A, 52, 415
Magnelli B. et al., 2012, A&A, 539, A155

Miville-Deschênes M.-A., Murray N., Lee E. J., 2017, ApJ, 834, 57

Narayanan D. et al., 2006, ApJ, 642, L107

Narayanan D. et al., 2015, Nature, 525, 496

Nims J., Quataert E., Faucher-Giguère C.-A., 2015, MNRAS, 447, 3612

Oh S. H., Kim W.-T., Lee H. M., 2015, ApJ, 807, 73

Oliver S. J. et al., 2010, A&A, 518, L21

Pearson J. C., Drouin B. J., 2006, ApJ, 647, L83

Planck Collaboration VI, 2020, A&A, 641, A6

Richard J., Kneib J. P., Limousin M., Edge A., Jullo E., 2010, MNRAS, 402, L44

Richard J. et al., 2014, MNRAS, 444, 268

Richings A. J., Faucher-Giguère C.-A., 2018a, MNRAS, 474, 3673

Richings A. J., Faucher-Giguère C.-A., 2018b, MNRAS, 478, 3100

Riechers D. A. et al., 2013, Nature, 496, 329

Rupke D., 2018, Galaxies, 6, 138

Salpeter E. E., 1955, ApJ, 121, 161

Schaye J. et al., 2015, MNRAS, 446, 521

Schroetter I. et al., 2019, MNRAS, 490, 4368

Shen S., Madau P., Guedes J., Mayer L., Prochaska J. X., Wadsley J., 2013, ApJ, 765, 89

Solomon P. M., Downes D., Radford S. J. E., Barrett J. W., 1997, ApJ, 478, 144

Somerville R. S., Davé R., 2015, ARA&A, 53, 51

Spitzer L., Jr., 1968, in Middlehurst B. M., Aller L. H., eds, Nebulae and Interstellar Matter. p. 1

Tacconi L. J. et al., 2008, ApJ, 680, 246

Tacconi L. J., Genzel R., Sternberg A., 2020, ARA&A, 58, 157

Tumlinson J., Peeples M. S., Werk J. K., 2017, ARA&A, 55, 389

Valdivia V., Godard B., Hennebelle P., Gerin M., Lesaffre P., Le Bourlot J., 2017, A&A, 600, A114

van der Tak F. F. S., Black J. H., Schöier F. L., Jansen D. J., van Dishoeck E. F., 2007, A&A, 468, 627

Veilleux S., Maiolino R., Bolatto A. D., Aalto S., 2020, A&AR, 28, 2

Verhamme A., Schaerer D., Maselli A., 2006, A&A, 460, 397

Vernet J., Cimatti A., 2001, A&A, 380, 409

Voit G. M. et al., 2020, ApJ, 899, 70

Walter F. et al., 2020, ApJ, 902, 111

Wright R. J., Lagos C. d. P., Power C., Mitchell P. D., 2020, MNRAS, 498, 1668

Yang C. et al., 2017, A&A, 608, A144

Zabl J. et al., 2019, MNRAS, 485, 1961

Zhang Z.-Y., Romano D., Ivison R. J., Papadopoulos P. P., Matteucci F., 2018, Nature, 558, 260

Zhuravleva I. et al., 2014, Nature, 515, 85

Zhuravleva I., Churazov E., Schekochihin A. A., Allen S. W., Vikhlinin A., Werner N., 2019, Nature Astron., 3, 832

APPENDIX A: THE CH$^+$ MANNA

CH$^+$ is a most fragile species: it has a highly endoenergic formation ($E_{form} \sim 0.4$ eV) and a fast destruction rate, by collisions with H and H$_2$. In diffuse and weakly irradiated gas, a warm chemistry activated by dissipation of turbulence in shocks and/or intense velocity shears has been proposed to overcome its fast destruction (Flower, Roueff & Zeippen 1998; Lesaffre et al. 2013; Godard et al. 2014). Turbulent transport in a biphase medium comprising a cold ($T \sim 100$ K) and a warm ($T \sim 10^4$ K) phase may also contribute to the CH$^+$ production in diffuse gas (Valdivia et al. 2017).

Once formed, its lifetime is so short,

$$t_{CH^+} = 1 \text{ yr } f(H_2)^{-1} \left(\frac{n_H}{50 \text{ cm}^{-3}} \right)^{-1}, \tag{A1}$$

that, unlike the CO molecule, CH$^+$, is always observed where it formed, i.e. it cannot be transported. Here, $f_{H_2} = 2n(H_2)/n_H$ is the H$_2$ fraction.

CH$^+$ being a light hydride with high dipole moment, the critical density ($\sim 10^7$ cm^{-3}) of its $J = 1$–0 transition is almost $10^5 \times$ larger than that of CO(1–0), so the line appears in absorption in low-density gas ($n_H < 10^3$ cm^{-3}). In emission, the CH$^+$ $J = 1$–0 line is detected only in dense and UV-illuminated gas, either photon-dominated regions (PDRs) or UV-irradiated shocks because, unlike most molecules, the abundance of CH$^+$ is enhanced in intense UV fields (Agúndez et al. 2010; Godard & Cernicharo 2013; Godard et al. 2019).

We recall here the method we devised in Paper I to infer the radius and mass of the reservoir of diffuse molecular gas from the observables: the radius r_{SMG} and flux of the sub-mm background continuum source and the width Δv_{abs} and opacity τ_0 of the CH$^+$ absorption line.

The dominant driver of CH$^+$ production in the diffuse gas causing the absorptions is assumed to be turbulent energy dissipation. As in a steady turbulent cascade, the energy dissipation and transfer rates balance each other, the dissipation rate per unit volume is $\bar{\epsilon} \propto \bar{\rho} \, \bar{v}_{turb}^3 / l$, where $l \sim r_{TR}$ and $\bar{\rho}$ are the unknown sizescale and mean mass density of the part of the turbulent reservoir sampled by absorption and $\bar{v}_{turb}$ is its mean turbulent velocity inferred from the width of the absorption line. Absorption lines provide the column density of CH$^+$ molecules and therefore the *number* of CH$^+$ molecules in the volume $\pi r_{SMG}^2 r_{TR}$ subtended by the background continuum source of radius r_{SMG} and the unknown length of the line-of-sight r_{TR} across the diffuse CGM. Because we know that these molecules formed in that volume (i.e. they cannot be transported), we know that the energy injection rate due to turbulent dissipation required to sustain the observed *number* of CH$^+$ molecules in that volume has to be

$$\dot{E}_{CH^+} = N(CH^+) \, \pi \, r_{SMG}^2 \, E_{form} \, / \, t_{CH^+}. \tag{A2}$$

It only depends on the observed absorption line (see equation 2) and the known values E_{form} and t_{CH^+}. The injection rate of turbulent energy in that same volume is

$$\dot{E}_{turb} = \bar{\epsilon} \times \pi r_{SMG}^2 \, r_{TR}, \tag{A3}$$

and a fraction α of this energy flux is feeding the warm chemistry:

$$\dot{E}_{CH^+} = \alpha \, \dot{E}_{turb}. \tag{A4}$$

An estimate $\alpha \sim 10^{-3}$ is inferred from CH$^+$ observations in the Milky Way as follows. The CH$^+$ abundances measured in the Solar Neighbourhood are about $3\times$ smaller than those measured in the inner Milky Way, at galactic radii between 4 and 6 kpc (Godard et al. 2014). An exponential decrease of the turbulent energy transfer rate ϵ is found between the Inner Galaxy and the Solar Neighbourhood from the analysis of CO(1–0) surveys, providing a similar ratio of the values of ϵ at these two galactic radii (Miville-Deschênes, Murray & Lee 2017). Since the turbulent cascade has been found to pervade the atomic medium and the molecular clouds down to the smallest non-star forming cores with a similar energy transfer rate $\epsilon \sim 2 \times 10^{-25}$ erg cm^{-3} s^{-1} in the Solar Neighbourhood (Falgarone, Hily-Blant & Levrier 2004), we assume that the same radial dependence applies to the entire cold interstellar medium (ISM):

$$X(CH^+) = N(CH^+)/N_{H,cool} = \kappa \epsilon, \tag{A5}$$

where $N_{H,cool} = N(H) + 2N(H_2)$ is the total column density of the cool hydrogen along the CH$^+$ lines-of-sight, $N(H)$ being provided by the 21cm absorption optical depth and $N(H_2)$ by CH and HF absorptions over the same velocity intervals (Godard et al. 2014). We find $\kappa = 10^{17}$ (erg cm^{-3} s^{-1})$^{-1}$ from the observed variations of

CH$^+$ abundances and ϵ with the Galactic radius. From equation (A4) adapted to the Galactic environment, we infer:

$$\alpha = \kappa \, \bar{n}_{\rm H,cool} \, \frac{E_{\rm form}}{t_{\rm CH^+}} \sim 10^{-3} \left(\frac{\bar{n}_{\rm H,cool}}{1\,{\rm cm}^{-3}} \right), \qquad (A6)$$

where $\bar{n}_{\rm H,cool}$ is the mean density of the cool diffuse ISM. An important assumption is made here: the same mean density is relevant for the turbulent energy transfer rate and the mean density of the gas in which CH$^+$ is observed in absorption. This is because the bulk of the gas mass is assumed to be that of the cool molecular phase ($T \sim 100$ K), while the bulk of the volume is filled with the warm phase ($T \sim 10^4$ K). This mean density is not the local density $n_{\rm H}$, involved in the collisional destruction rate of CH$^+$ (equation A1).

The gas mass contributing to the absorption is therefore

$$M_{\rm abs} = \mu_{\rm p} \, m_H \, N_{\rm H,cool} \, \pi \, r_{\rm SMG}^2, \qquad (A7)$$

where $\mu_{\rm p}$ is the mean mass per particle, and the turbulent energy flux pervading that mass, and eventually dissipated in the same volume, is

$$\dot{E}_{\rm turb} = \frac{1}{2} \, M_{\rm abs} \, \bar{v}_{\rm turb}^3 \, / \, r_{\rm TR}. \qquad (A8)$$

Using equation (A4), we then infer

$$X({\rm CH^+}) = \alpha \, \frac{\mu_{\rm p} \, m_{\rm H}}{2} \, \frac{t_{\rm CH^+}}{E_{\rm form}} \, \frac{\bar{v}_{\rm turb}^3}{r_{\rm TR}}. \qquad (A9)$$

The mass of the turbulent reservoir is then computed by assuming mass conservation across the different shells, regardless of the global inwards/outwards or turbulent motions, so that its average density decreases with radius as $\bar{n}_{\rm H} \propto r^{-2}$, for an assumed spherical geometry. In that case the hydrogen column density at impact parameter b decreases as $N_{\rm H}(b) \propto b^{-1}$ and the total gas mass is

$$M_{\rm TR} = 2 \, \pi \, \mu_{\rm p} \, m_{\rm H} \, r_{\rm TR} \, r_{\rm SMG} \, N_{\rm H,cool}, \qquad (A10)$$

where $N_{\rm H,cool}$ inferred from the CH$^+$ absorption lines is half the average hydrogen column density within the radius $r_{\rm SMG}$.

Introducing $r_{\rm TR} = \bar{v}_{\rm turb} \, t_{\rm SB}$, the total gas mass depends only on the absorption opacity, as shown in Paper I,

$$M_{\rm TR} = 3.8 \times 10^{10}\,{\rm M}_\odot \, \tau_0 \, t_{50}^2 \, r_{\rm SMG,kpc} \left(f_{\rm H_2} \frac{n_{50}}{\alpha_3} \right), \qquad (A11)$$

where we have introduced $\alpha_3 = \alpha/10^{-3}$, $t_{50} = t_{\rm SB}/50\,{\rm Myr}$ for the lifetime of the turbulent reservoirs, the local gas density $n_{50} = n_{\rm H}/50\,{\rm cm}^{-3}$ that determines the CH$^+$ lifetime. A mean mass per particle $\mu_{\rm p} = 1.27$ is adopted.

APPENDIX B: THE LENSING MODEL

SMM J02399−0136 is gravitationally lensed by the cluster Abell 370 (Ivison et al. 2010a). The mass distribution of this cluster has been studied in Richard et al. (2010) from the constraints given by 10 multiply lensed background sources observed with bands F475W/F625W and F814W from *HST*/ACS. These authors assumed for their lens model a bimodal pseudo-isothermal elliptical mass distribution. More recently, Diego et al. (2016) have found an alternative way of deriving a free-form mass distribution by analysing the latest *HST* Frontier images and GLASS spectroscopy. In general, different authors find a good consistency between different models taking into account two cluster clumps and taking independent subsamples of lensed sources as constraints. We recall that the goal of this work is to study the background source rather than to obtain a very detailed modelling of the lens. Since SMM J02399−0136 is

located far from the centres of these two cluster clumps, it is not strongly lensed and a simplification of the lensing model is justified.

In order to derive some of the intrinsic properties of the background source, we correct from the distortion and magnification of A370 using sl_fit (Gavazzi et al. 2011). This code adopts the standard Metropolis–Hastings algorithm, a standard Markov chain Monte Carlo (MCMC) method, to explore the space of parameters that best reproduces the observed data in the source plane. Given a set of parameters describing the lens model and the luminosity profile(s) of the background source(s), the code builds samples of the posterior probability distribution function of these parameters. We describe the lens as a singular isothermal ellipsoid (SIE) mass distribution centred on the cluster position obtained by Richard et al. (2010). We also fix the minor-to-major axial ratio $q_{\rm L}$ and orientation of the major axis in the plane of the sky (PA$_{\rm L}$) of the lens to 0.4 and 90.0 deg, respectively. To model the data in the background plane, we assume two sources and adopt an elliptical Sersic profile for their luminosity, leaving the rest of the parameters free. These include for each source q, PA, its relative position with respect to the lens centre, its effective radius, and its intrinsic flux.

We obtain a magnification factor $\mu = 1.9 \pm 0.1$ for L2SW and $\mu = 1.7 \pm 0.1$ for L1, in agreement with the range of values obtained in the literature (Section 1). We derive an effective radius of 0.22 ± 0.01 arcsec corresponding to a physical size of 1.8 ± 0.1 kpc for L2SW and a radius of 0.8 ± 0.1 kpc for L1, adopting for both the same redshift and the *Planck* cosmology ($H_0 = 67.4$, $\Omega_{\rm M} = 0.315$).

APPENDIX C: STATISTICAL SIGNIFICANCE OF THE CH$^+$ EMISSION STRUCTURES

As illustrated in Section 3.1, the tentative structures of CH$^+$ line emission are complex and not well suited to state-of-the-art statistical analysis of, e.g., continuum point-sources observed by ALMA. The statistical confirmation of their existence has to be conducted in space and velocity-space jointly, because the structures are highly dynamical (see Section 6.2) and their boundary and shape depend on the velocity range over which the line emission is integrated. They are spatially extended and often elongated with the shortest dimensions in some cases barely resolved. Their moment-0 values are comparable to the negative values of the minima visible in the moment-0 maps.

These negative spots can be understood as combined sidelobes of multiple extended weak sources, scattered in the ALMA primary beam. As an example, the conspicuous negative feature close to the phase centre (2 arcsec South of L2SW) and extending over ~ 2 ALMA synthesized beam is due to a very broad (FWHM = 2600 km s^{-1}) line with a peak intensity of -0.3 mJy. Such a large linewidth suggests that it results from the chance combination of negative sidelobes of multiple emissions of narrower width. The order of magnitude of its intensity can be recovered for a total extent of the eight central structures of average size $\overline{\Omega} = 0.49$ arcsec^2, equivalent to $8 \times 0.49/0.17 = 23$ synthesized beams, an average linewidth of 1330 km s^{-1} and an average flux of 0.2 mJy (Table 2): the combination of the sidelobes of 16 of these synthesized beams would be enough.

To assess the reality of an excess of extended positive structures in the moment-0 maps and its dependence on the distance to the centre of phase, we have identified in four moment-0 maps ensembles of neighbouring pixels brighter than $\sigma_{\rm m0}$ (or weaker than $-\sigma_{\rm m0}$) and connected over areas more extended that one ALMA synthesized beam. In Fig. C1, the excess number of pixels with positive moment-0 values over those with negative values, normalized to the total
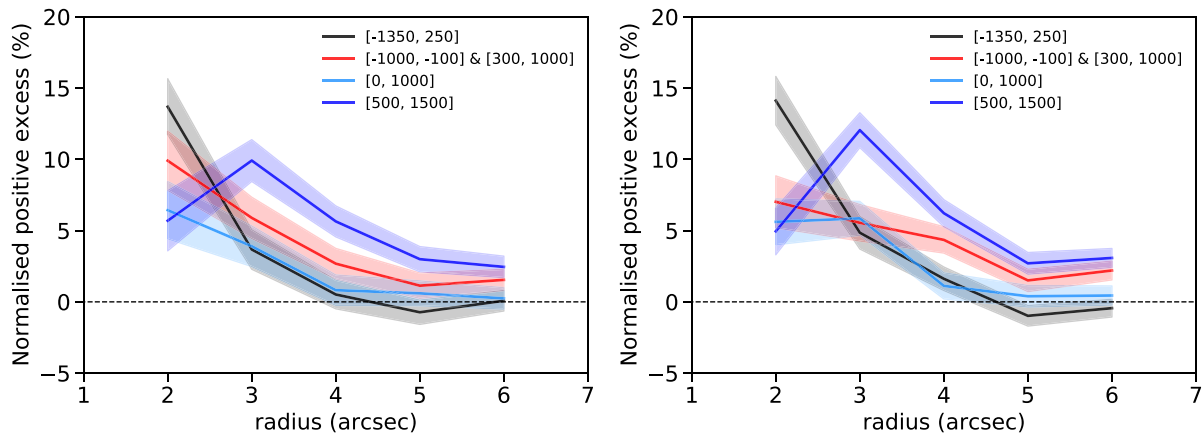
Figure C1. Radial dependence of the excess of positive moment-0 pixels over those with negative values as a function of the radius (i.e. distance to the phase centre) for all the structures (left) and those larger than one synthesized beam (right). The difference is normalized to the total number of pixels within a given radius. Four moment-0 maps have been analysed, characterized by their velocity coverage (upper right corners). The shaded areas correspond to $\pm 2\sigma$ rms.
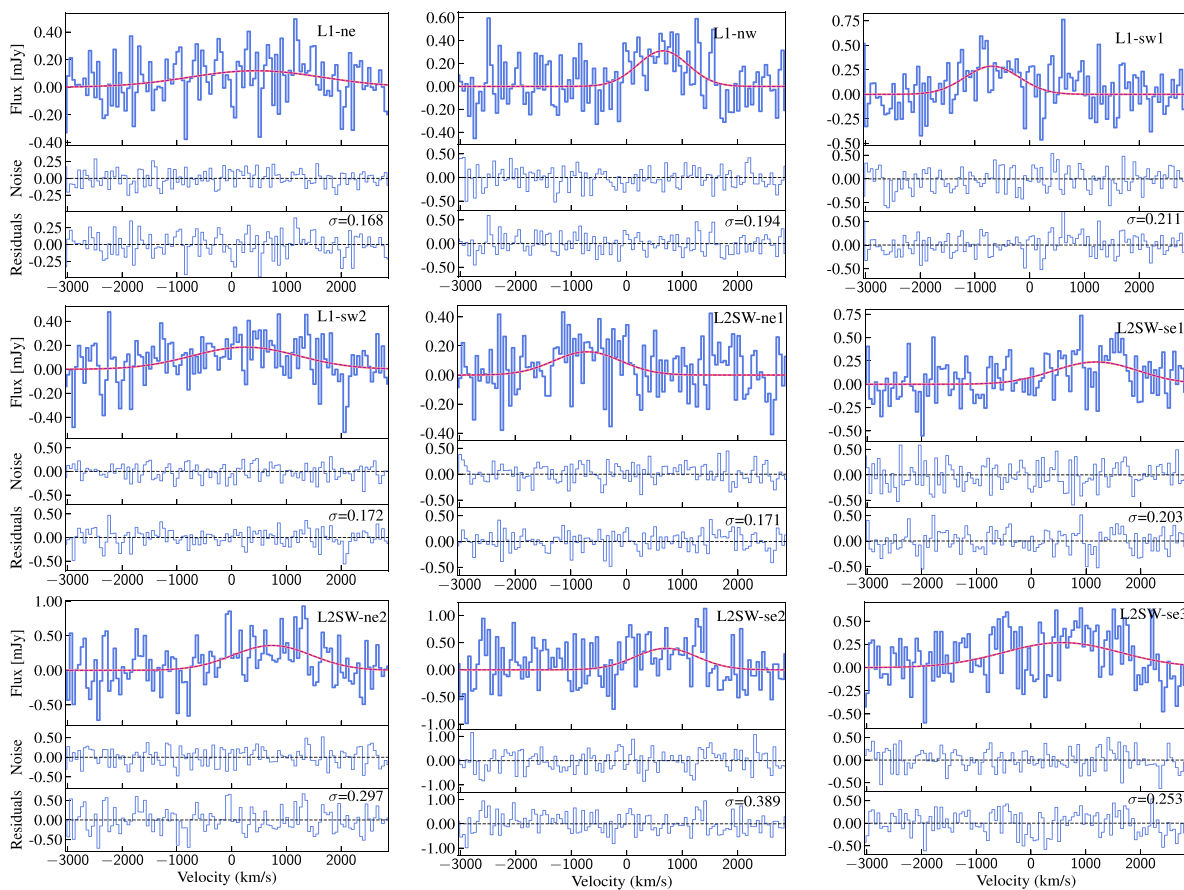

Figure C2. Same spectra as those of Fig. 3 with the additional noise spectrum taken within the same shape as that of each CH$^+$ emission structure, but localized in its vicinity. Note that the flux scales of the noise spectra and the residuals are the same for a given structure.

number of pixels within a given radius, is displayed as a function of this radius (i.e. the distance to the phase centre). The left-hand panel displays this excess for all the connected structures above σ_{m0} (and weaker than $-\sigma_{m0}$), whatever their size, and the right-hand panel considers only the pixels in structures larger than one synthesized beam area. In the latter case, the excess of positive structures above

those negative is statistically significant within 4.5 arcsec from the phase centre. This limit depends on the moment-0 map, as the positive excess computed over [500, 1500] km s^{-1} remains significant up to a distance of 6 arcsec. This velocity interval corresponds to the velocity range where the CH$^+$ emission is the most intense (Fig. 6).

Last, Fig. C2 displays the same spectra as in Figs 3 and 4, but those of L1-s and L2SW-n, with an additional spectrum taken within a similar contour as that of each CH^+ emission structure, localized in its vicinity. These spectra illustrate the excellent quality of the ALMA baselines.

APPENDIX D: RESULTS OF CH^+ NON-LTE RADIATIVE TRANSFER

The average CH^+ peak emission line brightness of the 13 kpc-scale shocks identified in the field is 0.07 mJy beam^{-1} inferred from their average flux density, 0.25 mJy, and solid angle 0.75 arcsec^2, or ~ 3.6 beams (Table 3). We express this line brightness in mean brightness temperature, following the basic expressions of the line luminosity in the distant Universe (Solomon et al. 1997). At the redshift of the source $z = 2.8041$, we find that

$$1\,\text{mJy beam}^{-1} = 1.4 \times 10^7 \frac{\lambda^2[m]}{b_1[''] \times b_2['']}\,\text{mK}, \qquad (D1)$$

where λ is the observed wavelength and $b_1[''] \times b_2['']$ the synthesized beam. The mean $CH^+(1-0)$ line brightness of the extended sources detected by ALMA is therefore $T_R \sim 10$ mK.

The results of non-LTE radiative transfer computed with RADEX (van der Tak et al. 2007) are displayed in Fig. D1 for two CH^+ column densities and a velocity dispersion $\sigma_v = 20\,\text{km s}^{-1}$ representative of the intermediate velocity molecular shock models we consider (Godard et al. 2019; Lehmann et al. 2020a). Densities larger than $n_H = 10^4$ cm^{-3} are required to produce the line intensities, even at high temperatures. The black curves correspond to the line temperature at which $T_{ex} = T_{cont}$, where T_{ex} is the line excitation temperature and T_{cont} is the temperature of the continuum background source. These lines separate the parameter domain where the line is seen in emission from that where it is seen in absorption against the continuum background. The lines drawn here, $T_R = 1$ mK, are computed for $T_{cont} = 2$ K. For the smaller continuum fluxes of L1 and L2SW, the curves separating absorption from emission are at ~ 0.1 mK in the middle of the green area.
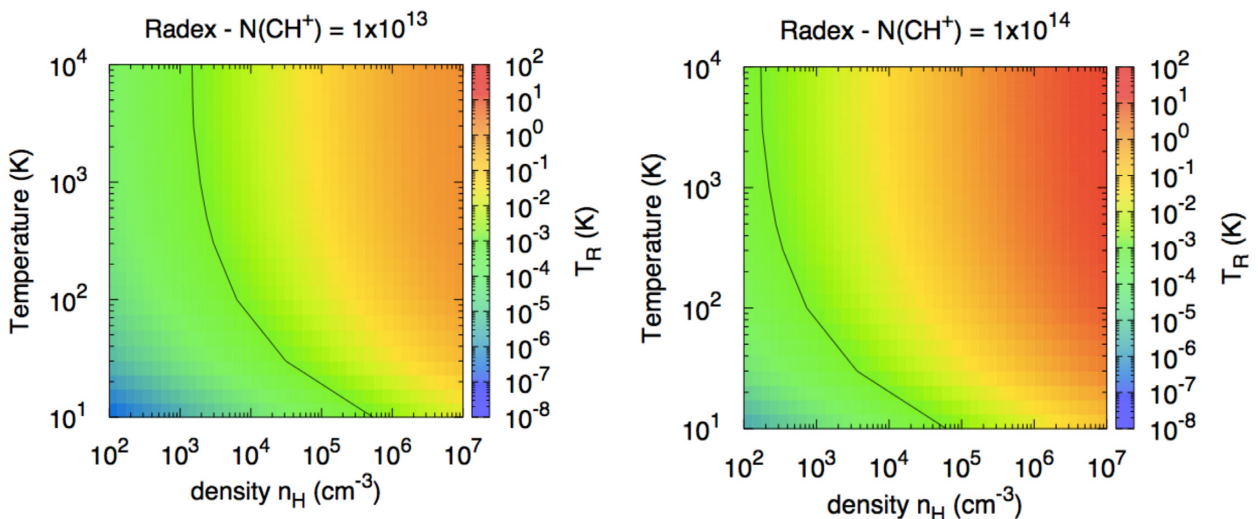
APPENDIX E: FURTHER COMPARISON OF THE CH^+ AND HIGH-VELOCITY LYα EMISSIONS

Smoothed versions of selected moment-0 maps are compared with the high-velocity Lyα contours in Fig. E1. The smoothed moment-0 maps are not computed as a spatial convolution of the moment-0 maps, with a beam twice larger than the original resolution, but on the original continuum-subtracted spectra. This is why the maps of Fig. E1 do not look like a spatially smoothed version of those of Figs 2–4. These figures show that the CH^+ emission structures identified in the native resolution moment-0 maps are indeed connected by large and weaker structures that exquisitely follow the contours of the high-velocity Lyα maps. We stress the following features:

(i) the elongated NE-SW feature across L1 in the $[-1000, -100]$ and $[300, 1000]$ km s^{-1} moment-0 maps comprises L1-ne, L1-em, L1-sw1, and L1-sw2 and is parallel to the broad orientation of the $[1000, 1500]$ km s^{-1} Lyα contours,

(ii) L1-nw, L1-ne, and L1-sw1 are parts of a ring in the $[500, 1500]$ km s^{-1} moment-0 map that closely follows the edge of the red HV Lyα contours,

(iii) same kind of coincidence for L2SW-se2 in the $[0, 1000]$ km s^{-1} moment-0 map and L2SW-em in the $[-1350, 250]$ km s^{-1} moment-0 map with the red HV Lyα contours,

(iv) L2SW-se3, L2SW-se2, L2SW-ne1 located at the tip of elongated structures in the red HV Lyα map,

(v) a weak and elongated lane in the $[500, 1500]$ moment-0 map follows the northern edge of the blue HV Lyα contours as does L2SW-ne2 at their South-Eastern edge.

There are a few additional structures that have not been selected, such as that 2 arcsec south of L2SW in the $[-1000, -100]$ and $[300, 1000]$ km s^{-1} moment-0 map, but as said in Section 3.1, the goal of this selection is not to make a complete census of all the CH^+ emission spots detected by ALMA but to shed light on a specific process, namely the molecular shocks at the interface of the CGM and outflows, seen as positive and negative high-velocity Lyα emission.

Figure D1. $CH^+(1-0)$ line temperatures, T_R, from non-LTE radiative transfer using RADEX (van der Tak et al. 2007) for two CH^+ column densities $N(CH^+)$ $= 10^{13}$ (left) and $N(CH^+) = 10^{14}$ cm^{-2} (right) and broad ranges of local hydrogen density n_H and gas temperature T. The black lines at $T_R = 1$ mK separate the parameter domains, where the line is seen in emission from that where it is seen in absorption against a continuum of temperature $T_{cont} = 2$K, a value relevant for the bright sources of Paper I. For the fainter SMG SMM J02399−0136, this boundary is at $T_R \approx 0.1$ mK.

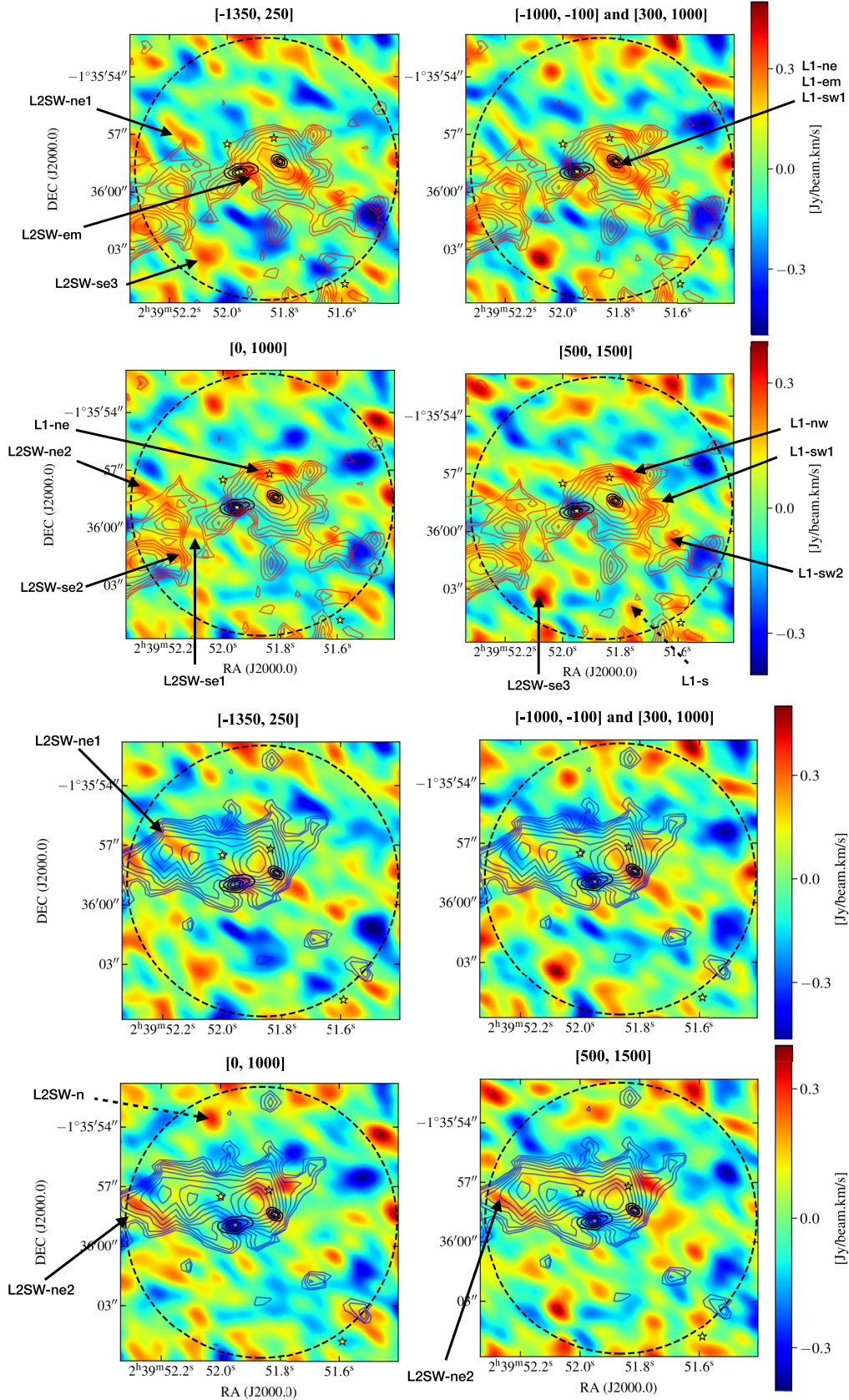**Figure E1.** Smoothed moment-0 maps computed over the velocity range indicated at the top of each panel, superposed to the Lyα brightness integrated over [1000, 1500] km s^{-1}, (red contours) (top panels) and over [−1200, −700] (blue contours) (bottom panels).

This paper has been typeset from a TEX/LATEX file prepared by the author.